Thermo-viscoplastic behavior of 304 austenitic stainless steel at various strain rates and temperatures: Testing, modeling and validation

B. Jia [a,b,*], A. Rusinek [c,d,e], R. Pesci [b], S. Bahi [c], R. Bernier [c]

[a] ENSAM-Arts et Métiers ParisTech, Laboratory of Design, Manufacturing and Control (LCFC), Metz 57070, France
[b] ENSAM-Arts et Métiers ParisTech, Laboratory of Microstructure Studies and Mechanics of Materials (LEM3), UMR CNRS 7239, Metz 57078, France
[c] Lorraine University, UFR MIM, Laboratory of Microstructure Studies and Mechanics of Materials (LEM3), UMR CNRS 7239, Metz 57078, France
[d] Institute of Fundamental Technological Research, Ul. Pawinskiego 5B, Warsaw 02-106, Poland
[e] Chair of Excellence, Departamento de Ingeniería Mecánica, UC3M (Carlos III University, Madrid) Avda. de la Universidad 30, Leganés, Madrid 28911, Spain

A B S T R A C T

This paper presents a systematic study of the thermo-viscoplastic behavior of a 304 austenitic stainless steel (ASS). The experiments were conducted over a wide range of strain rates (10^{-3} s^{-1} to 3270 s^{-1}) and temperatures (-163°C to 172°C), for which the deformation behavior of 304 ASS becomes more complex due to the strain-induced martensitic transformation (SIMT) effect. Dynamic tests at low/elevated temperatures were conducted using the Hopkinson technique coupled with a cooling device/heating furnace, and temperature distribution within the specimen was verified to be uniform. Experimental results showed that the strain hardening rate of 304 ASS was strongly affected by SIMT effect. For quasi-static tests (10^{-3} s^{-1} to 1 s^{-1}) at low temperatures (-163°C to -20°C), the stress-strain relations exhibited an S-shape and a second strain hardening phenomenon. The strain rate sensitivity and temperature sensitivity of 304 ASS were also different from metallic materials deformed by dislocation glide. Several unexpected phenomena including the negative strain rate sensitivity and the changing temperature sensitivity from quasi-static to dynamic tests were observed. Based on experimental results, an extension of the Rusinek-Klepaczko (RK) model considering SIMT effect was used to simulate the deformation behavior of 304 ASS: it predicted flow stress curves of 304 ASS above -60°C correctly. In addition, to validate the extended RK model and the identified model parameters, numerical simulations of ballistic impact tests of 304 ASS plates at various temperatures were carried out, showing a good agreement with experiments.

1. Introduction

As a representative of transformation induced plasticity (TRIP) steels [1], 304 ASS has a unique combination of high strength and high ductility [2]. Its beneficial mechanical properties come from the SIMT effect, which means that upon plastic deformation process the initial austenite phase (γ) transforms into the stable martensite phase (α'); thus, both improved work hardening rate and significantly enhanced ductility can be achieved. 304 ASS is widely used in many engineering areas ranging from liquefied natural gas storage at cryogenic temperatures [3,4] to crash-resistant structures in automotive industry at room temperature [5,6] and nuclear facilities at elevated temperatures [7]. Therefore, much work has been done to investigate the deformation behavior of 304 ASS under various strain rates and temperatures.

The effect of temperature on the deformation behavior of 304 ASS is different from the commonly used alloys with the deformation mechanism of dislocation glide. As shown in Fig. 1, at temperatures lower than M_d, the temperature below which martensitic transformation occurs automatically or can be triggered by plastic deformation [5,6], stress-strain relations of 304 ASS exhibit an S-shape and a second hardening phenomenon. This is caused by the martensitic transformation effect. At temperatures above M_d, the deformation mechanism of 304 ASS changes into dislocation glide [5]. With increasing temperature, dislocation annihilation due to the cross slip and climb of dislocations is accelerated [8]; thus the strength of 304 ASS decreases without the second hardening phenomenon. Byun et al. [9] studied the quasi-static tension behavior of 304 ASS at temperatures between −150°C and 450°C. It was observed that both the yield stress and the ultimate tensile strength decreased with increasing temperature T_0, and the optimal ductility peaked at 20°C. At temperatures lower than 20°C, a second hardening phenomenon accompanied by martensitic transformation was observed. Hamada et al. [10] investigated the quasi-static deformation behavior of 201 and 201 L austenitic stainless steels at temperatures ranging from −80°C to 200°C and obtained similar results: the flow stress increases with decreasing temperature. Zheng and Yu [11] studied the quasi-static tension behavior of 304 ASS at temperatures between −253°C and 20°C and found that both the flow stress and the strain hardening rate increased with decreasing

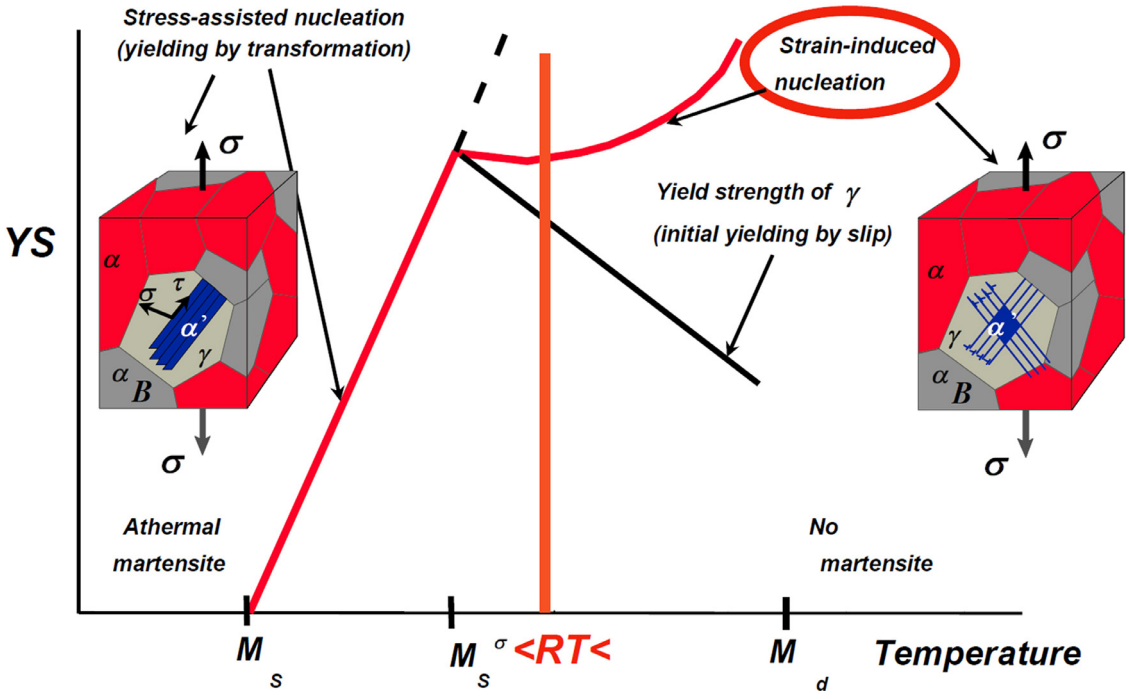


Fig. 1. Schematic illustration of the deformation mechanism of TRIP steels at different temperatures: stress assisted plasticity ($M_s - M_s^\sigma$), strain-induced plasticity ($M_s^\sigma - M_d$), and dislocation glide plasticity ($> M_d$) [12].

temperature. In addition, due to the thermally induced martensitic transformation before tests, the yield stresses at −253°C and −196°C were significantly higher than for the other temperatures.

The effect of strain rate on the deformation behavior of 304 ASS can be explained in two strain regimes: at the initial stage of deformation, the constitutive behavior of 304 ASS is dominated by dislocation slip. The flow stress increases with increasing strain rate as the time available for a dislocation to wait in front of an obstacle for the additional thermal energy is reduced [8,13]. However, when it comes to large strains, the strengthening effect originated from SIMT is inhibited by adiabatic heating, and the corresponding strain hardening rate decreases. Considering the effects of strain rate on both dislocation slip and SIMT, either positive [14,15] or negative [3,16] strain rate sensitivity at large strains was observed. Lichtenfeld et al. [17] investigated the tension behavior of 304 L stainless steel under various strain rates (10^{-4} s^{-1} to 4×10^2 s^{-1}) at room temperature. The yield stress increased continuously with increasing strain rate. However, the ultimate strength declined first in quasi-static strain rates (10^{-4} s^{-1} to 10^{-2} s^{-1}) and then began to increase in dynamic strain rates (10^{-1} s^{-1} to 4×10^2 s^{-1}). A similar phenomenon was observed by Ishikawa and Tanimura [18] in 304 N stainless steel.

From the literature review, the deformation behavior of 304 ASS has been investigated massively. Previous studies mainly focused on quasi-static behavior at various temperatures or dynamic behavior at room temperature. Although the combined effects of temperature and dynamic loading on mechanical properties of 304 ASS are frequently encountered such as liquefied natural gas storage (−163°C) and sheet metal forming (20°C to 300°C), the corresponding deformation behavior is not clearly understood. In addition, at temperatures above M_d, the deformation behavior of 304 ASS is similar to that of the commonly used steels. However, at temperatures lower than M_d, the deformation behavior of 304 ASS becomes complex due to the SIMT effect. Hence, a deformation behavior study of 304 ASS especially focusing on temperatures below M_d (140°C for the studied material) can be interesting.

In this paper, the compression behavior of 304 ASS has been studied over a wide range of strain rates and temperatures. In industrial applications, strain rates can reach 2000 s^{-1} with a common regime lying around 10^{-3}–10 s^{-1} [19]. Considering the strain rate limitations of the adopted SHPB technique and the flow stress level of the studied 304 ASS, four quasi-static strain rates (10^{-3} s^{-1}, 10^{-2} s^{-1}, 10^{-1} s^{-1} and 1 s^{-1}) and three dynamic strain rates (1550 s^{-1}, 2370 s^{-1}, 3270 s^{-1}) were selected. For the testing temperature, much work concerning deformation behavior of 304 ASS at room or high temperature can be found, but studies at lower temperature is rare. In this work, six temperatures covering low temperature (−163°C, −60°C and −20°C), room temperature (20°C) and temperatures respectively below M_d (88°C) and slightly higher than M_d (172°C) were considered.

First, self-designed heating furnace and cooling device are coupled to the conventional SHPB device for dynamic compression tests not only at low but also at elevated temperatures. The set-up reliability is verified by both experiments and numerical simulations. Then, compression tests of 304 ASS have been conducted and the effects of temperature and strain rate on the deformation behavior of 304 ASS are discussed in detail. An extension of the Rusinek–Klepaczko (RK) constitutive model [20,21] considering martensitic transformation is chosen to describe the temperature and strain rate-dependent constitutive behavior. Finally, to verify the prediction capability of the extended RK model, numerical simulations of ballistic impact tests of 304 ASS have been carried out and compared to experiments.

2. Material behavior and set-up description

2.1. Material and specimens

The material considered herein is a commercial 304 stainless steel produced by Thyssenkrupp Materials, available in annealed plates (dimensions: 1000×100×12 mm^3). According to the manufacturer's specification, the chemical composition of the steel is given in Table 1.

Table 1
Chemical composition of the 304 ASS given by the supplier (wt%).

Material	C	Cr	Mn	N	Ni	Co	Cu	Fe
304 ASS	0.018	17.60	1.64	0.72	8.04	0.20	0.33	Bal

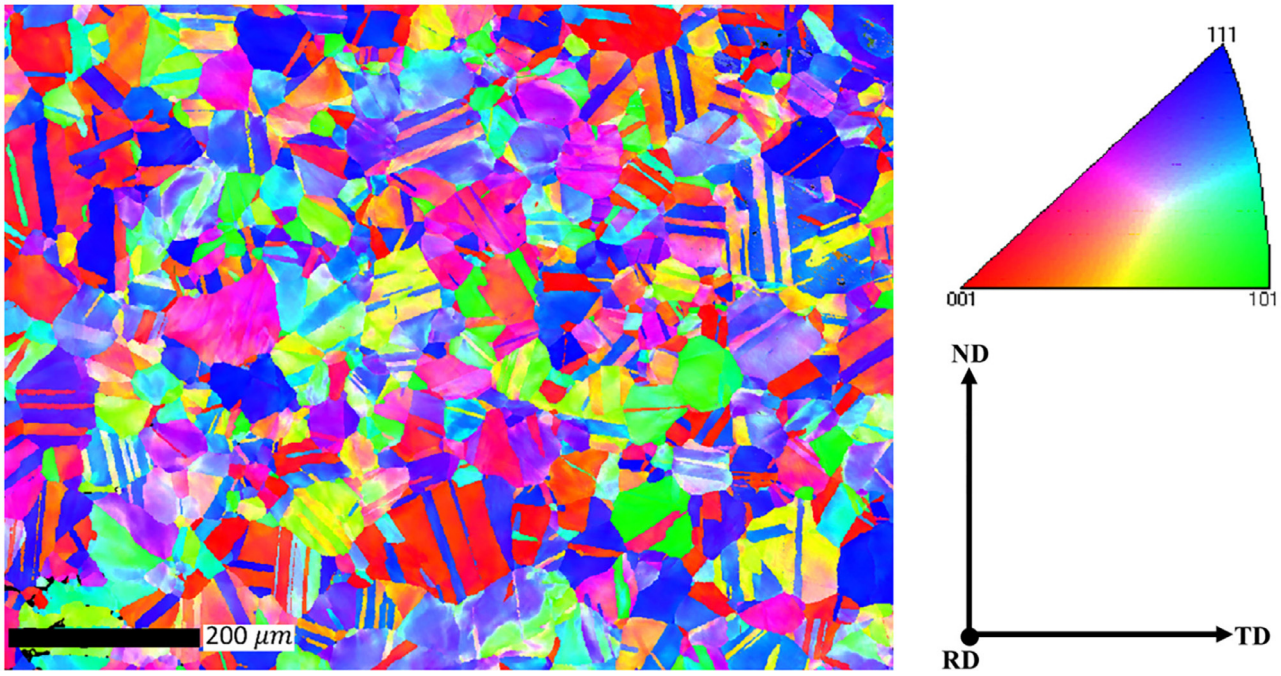


Fig. 2. The normal direction IPF of 304 ASS.

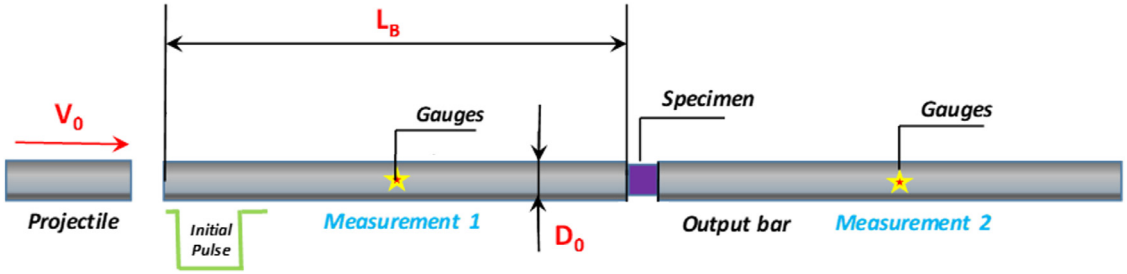


Fig. 3. Schematic diagram of the conventional SHPB set-up.

The microstructure of the 304 ASS was characterized by electron backscatter diffraction (EBSD) technique. By applying a step size of 1 μm and considering a misorientation angle of 5°, the normal direction inverse pole figure (IPF) is shown in Fig. 2. It is seen that the 304 ASS consists of 100% austenite phase with an average grain size of 28 μm.

The specimens used for compression tests are cylinders 3 mm high and 6 mm in diameter. As reported in [22], a height to diameter ratio of s_0=0.5 helps to reduce the friction and the inertia effects. The specimens were machined from the as-received plate along the rolling direction using wire electrical discharge machining (WEDM) technique. To avoid buckling and to ensure a uniform stress state inside the specimens, the specimen end faces were coated with lubricant. To ensure the reliability of the experimental results, three tests were performed for each temperature and strain rate combination. The average curve for each condition is depicted as the reference in this work.

2.2. Quasi-static and dynamic compression tests

Quasi-static tests at room temperature were conducted using a Zwick/Roell 200 kN universal testing machine. For tests at low and high temperatures, a cooling device or a heating furnace was used.

To study the dynamic behavior of 304 ASS, compression tests with average strain rates around 10^3 s^{-1} and initial temperatures varying between −163°C and 172°C were carried out using an SHPB set-up. The SHPB device, Fig. 3, consists of two long elastic bars (length of L_B = 1500 mm and diameter of D_0 = 20 mm), a compression specimen sandwiched between them and a projectile. When the projectile impacts the input bar with an initial velocity V_0, an incident wave $\varepsilon_I = \rho C_0 V_0/2E$ is induced with a celerity $C_0 = \sqrt{E/\rho}$ (E and ρ are Young modulus and density of the SHPB bars, respectively). Due to the cross-section difference and the mechanical impedance between the bars and the specimen, part of the incident wave is reflected back as $\varepsilon_R(t)$ and the rest transfers into the second bar as $\varepsilon_T(t)$. Using the three waves measurement, the average stress-strain relations of the tested material may be determined. A complete description of the stress wave analysis to define material behavior may be found in [23].

For dynamic tests at elevated temperatures, a heating furnace coupled to the conventional SHPB set-up is adopted. An illustration of the furnace is shown in Fig. 4. During the heating process, the specimen together with part of the incident and transmitter bars are heated. Two thermocouples are used to monitor the temperature of the specimen and the furnace environment, respectively; the latter can provide feedback to the temperature controller to adjust the heating rate. The maximum testing temperature by the heating furnace is close to 250°C.

Concerning dynamic tests at low temperatures, a cooling device based on pulsed cryogenic gas method has been developed, Fig. 5(a). The cold nitrogen gas flows from a liquid nitrogen tank through an aluminum pipe into the cooling box. The temperature inside the cooling box is monitored by a thermocouple connected to a temperature controller. Once the environmental temperature reaches the set value, the temperature controller cuts off the power of the pump to stop the

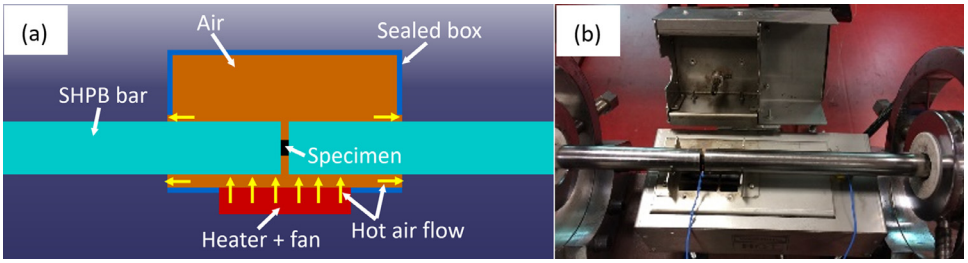


Fig. 4. Heating furnace for high temperature tests: (a) a schematic illustration and (b) the complete device.

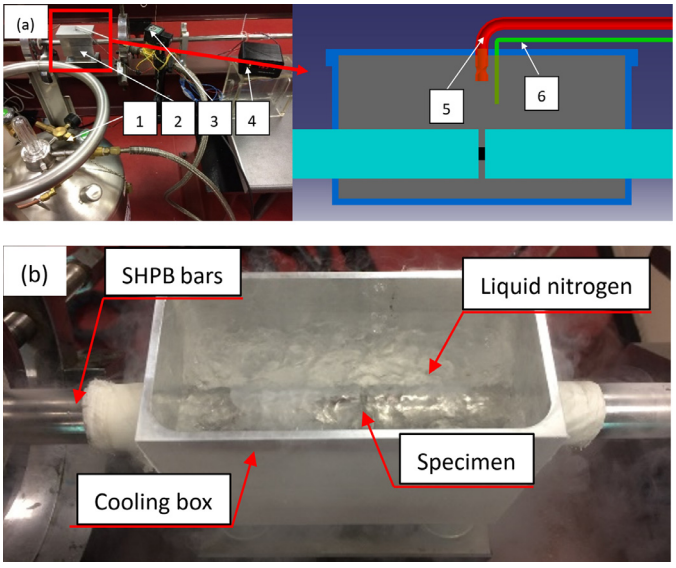


Fig. 5. Cooling device for low temperature tests: (a) between −90°C and −20°C and (b) −163°C. 1) liquid nitrogen tank, 2) cooling box, 3) pump for nitrogen gas flow, 4) temperature controller, 5) pipe for the nitrogen gas flow, 6) thermocouple.

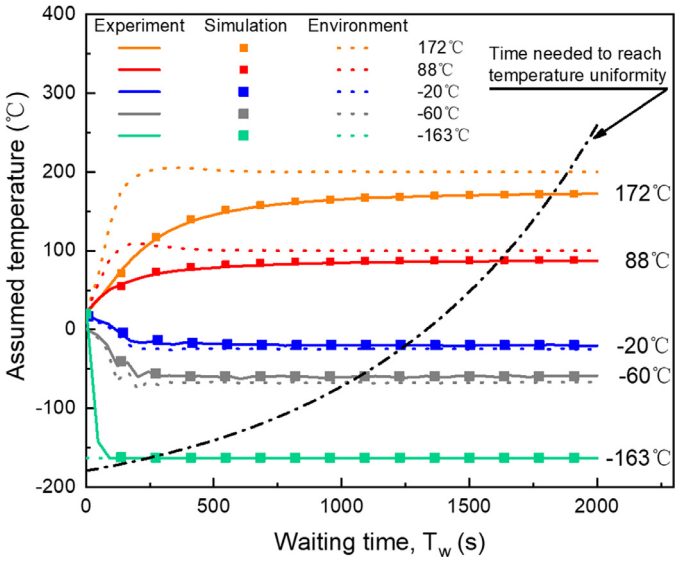


Fig. 6. Temperature evolution in the specimen with the environmental temperature varies between −163°C and 200°C.

nitrogen gas flow. By this method, the temperature varies precisely from −90°C to −20°C. In addition, to decrease strongly the initial temperature, the cooling box is filled with liquid nitrogen directly. By this method, a minimum temperature of −163°C can be reached.

Since the heating furnace and cooling device for high/low temperature tests are home-developed, their reliability should be checked before testing. Hence, the temperature evolution of the heating furnace/cooling device has been measured experimentally and is presented in the next section. In addition, the temperature distribution inside the specimen was further estimated by finite element method (FEM) based on thermal heat transfer approach.

3. Calibration and heat transfer modeling of the heating furnace/cooling device

The temperature evolution of the specimen and the environment is measured experimentally, and the result is shown in Fig. 6. By setting the environmental temperatures of the heating furnace/cooling device to be 200°C, 100°C, −25°C, −68°C and −163°C, the corresponding temperatures of the specimen are 172°C, 88°C, −20°C, −60°C and −163°C. The waiting time T_w for the specimen temperature to be stable changes depending on the initial temperature T_0. It increases from T_w=270 s at −163°C continuously to T_w=1820s at 172°C. By changing the environmental temperature of the heating furnace/cooling device between −163°C and 200°C, the corresponding temperature in the specimen varies from −163°C to 172°C.

To analyze the temperature distribution in the heating furnace/cooling box more precisely, numerical simulations using COMSOL Multiphysics have been conducted. The thermal transfer is described by the generalized transient heat equation, Eq. 1.

$$\rho.C_p(T).\frac{\partial T}{\partial t} - \nabla.(k(T).\nabla T) = 0 \tag{1}$$

The thermal conductivity $k(T)$ and the specific heat $C_p(T)$ of 304 ASS may be found in [24]. The boundary conditions are defined in Eq. (2) and Fig. 7.

- Natural convective heat flux q_c on the free surfaces of the heating furnace/cooling device and the SHPB bars.
- Forced convective heat flux q_f through the free surfaces of the specimen and the SHPB bars by hot air, cold nitrogen gas or liquid nitrogen.
- Thermal contact heat flux q_{int} between interfaces of the specimen and the SHPB bars.
- Hot air inflow and outflow with certain temperatures and velocities.

$$\begin{cases} q_c = -h_c\left(T - T_0\right) \ in \ \partial\Omega_c \\ q_f = -h_f\left(T - T_0\right) \ in \ \partial\Omega_f \\ q_{int} = h_{int}\left(T - T_0\right) \ in \ \partial\Omega_{int} \end{cases} \tag{2}$$

where $h_c = 10\ W/(m^2 \bullet K)$ and $h_{int} = 10^5\ W/(m^2 \bullet K)$ are the natural heat convection and the layer conductance coefficient, respectively. Values of h_c and h_{int} may be found in [25]. The forced heat convection coefficient h_f is equal to 818 $W/(m^2{\cdot}K)$ when cooling down the specimen by liquid nitrogen and 109 $W/(m^2{\cdot}K)$ when nitrogen gas or hot air is used. Values of h_f were obtained by fitting numerical results to the experimental data.

A comparison of temperature evolution between experiments and numerical simulations is shown in Fig. 6. It is clear that a good agreement is obtained for all the five temperatures. Therefore, the numerical

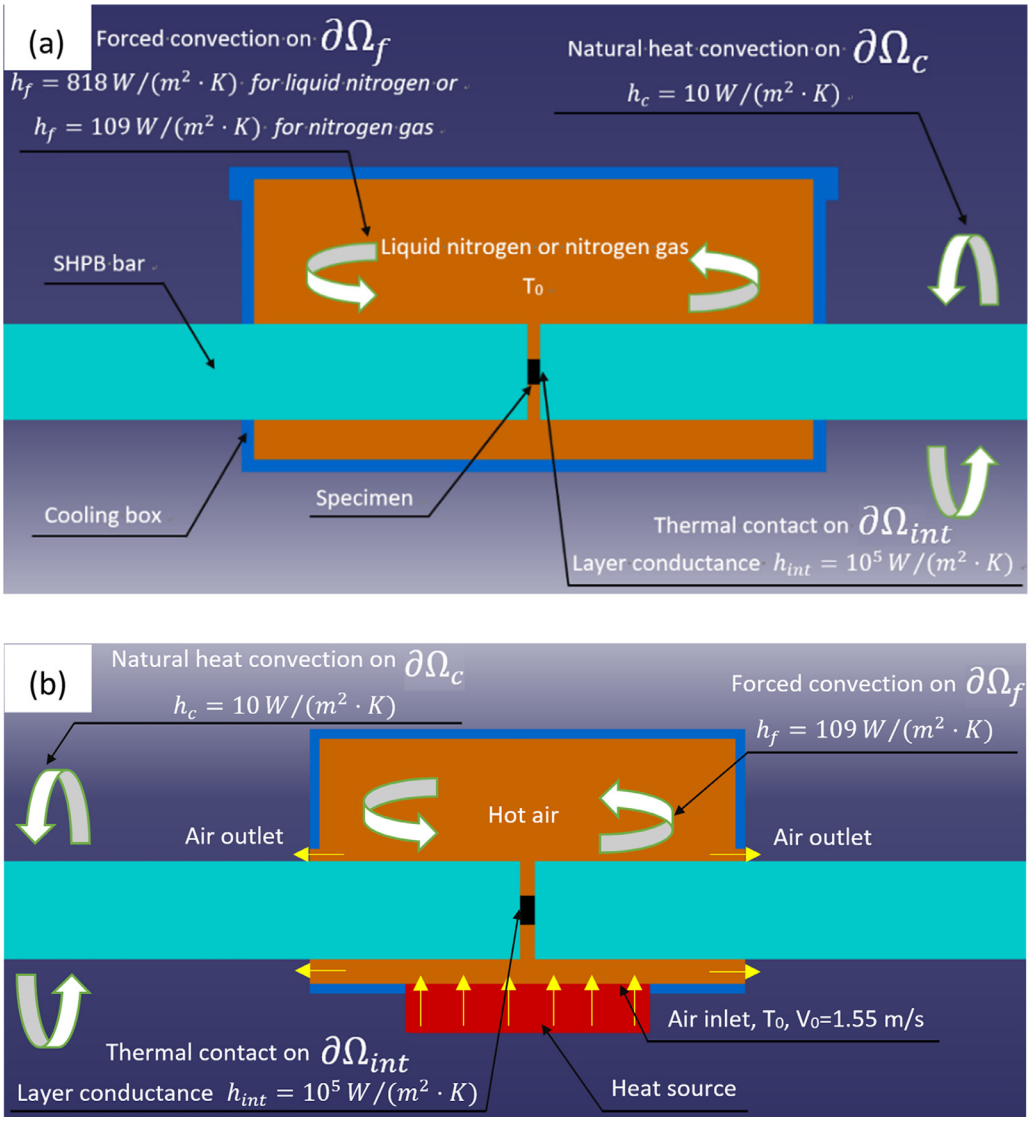


Fig. 7. Boundary conditions for temperature distribution analysis using COMSOL Multiphysics: (a) low temperature and (b) elevated temperature.

simulations can predict the temperature evolution and distribution of the heating furnace/cooling device correctly.

Based on the numerical results, the temperature evolution of four positions shown in Fig. 8(a) was recorded; the results are then plotted in Fig. 8(b). It is seen that temperatures in points A and B are always the same, indicating a uniform temperature distribution within the specimen. In comparison, temperatures in points C and D are lower due to the heat exchange between the SHPB bars and the environment. The temperature difference between the four points increases when the testing temperature deviates obviously from room temperature, and a strong temperature gradient along the SHPB bars is observed for T_0= −163°C and 200°C.

According to Fig. 8(b), the temperatures in the four positions are stable after a waiting time of 2000s. At T_w=2000s, the temperature distribution of the specimen and the environment is shown in Fig. 9. For tests at low temperatures, as shown in Fig. 9(a), (b) and (c), a strong temperature gradient forms along the SHPB bars, but the temperature distribution within the specimen is uniform with a maximum fluctuation of 0.05°C. For tests at elevated temperatures, as shown in Fig. 9(d) and (e), a temperature gradient is observed from the bottom to the top of the heating furnace, but the temperature within the specimen remains uniform with a fluctuation of 1.2°C.

4. Experimental results and discussion

4.1. Force equilibrium state within the specimen

The typical wave signals from one test at 1564 s^{-1} and 172°C are shown in Fig. 10(a). In order to obtain an accurate deformation behavior description using the SHPB technique, force equilibrium state within the specimen is necessary. Hence, a parameter proposed by Ravichandran and Subhash, $R(t)$, is used to evaluate the force equilibrium condition.

$$R(t) = \left|\frac{\Delta F(t)}{F_{avg}(t)}\right| = 2\left|\frac{F_1(t) - F_2(t)}{F_1(t) + F_2(t)}\right| \tag{3}$$

where $F_1(t)$ and $F_2(t)$ are the two forces acting on the end faces of the specimen, respectively. They are calculated as $F_1(t) = EA(\varepsilon_I(t) + \varepsilon_R(t))$ and $F_2(t) = EA\varepsilon_T(t)$, where E and A are Young's modulus and the cross-sectional area of the SHPB bars, respectively. $\Delta F(t)$ and $F_{avg}(t)$ are respectively the difference and the average of the two forces. A force equilibrium state is achieved when $R(t)$ is close to zero.

Based on the experimental results in Fig. 10(a), the variation of true stress, strain rate and force equilibrium coefficient with true strain is calculated and shown in Fig. 10(b). It can be seen that $R(t)$ is always lower than 0.1, except a fluctuation at a true strain of 0.02. Therefore, force

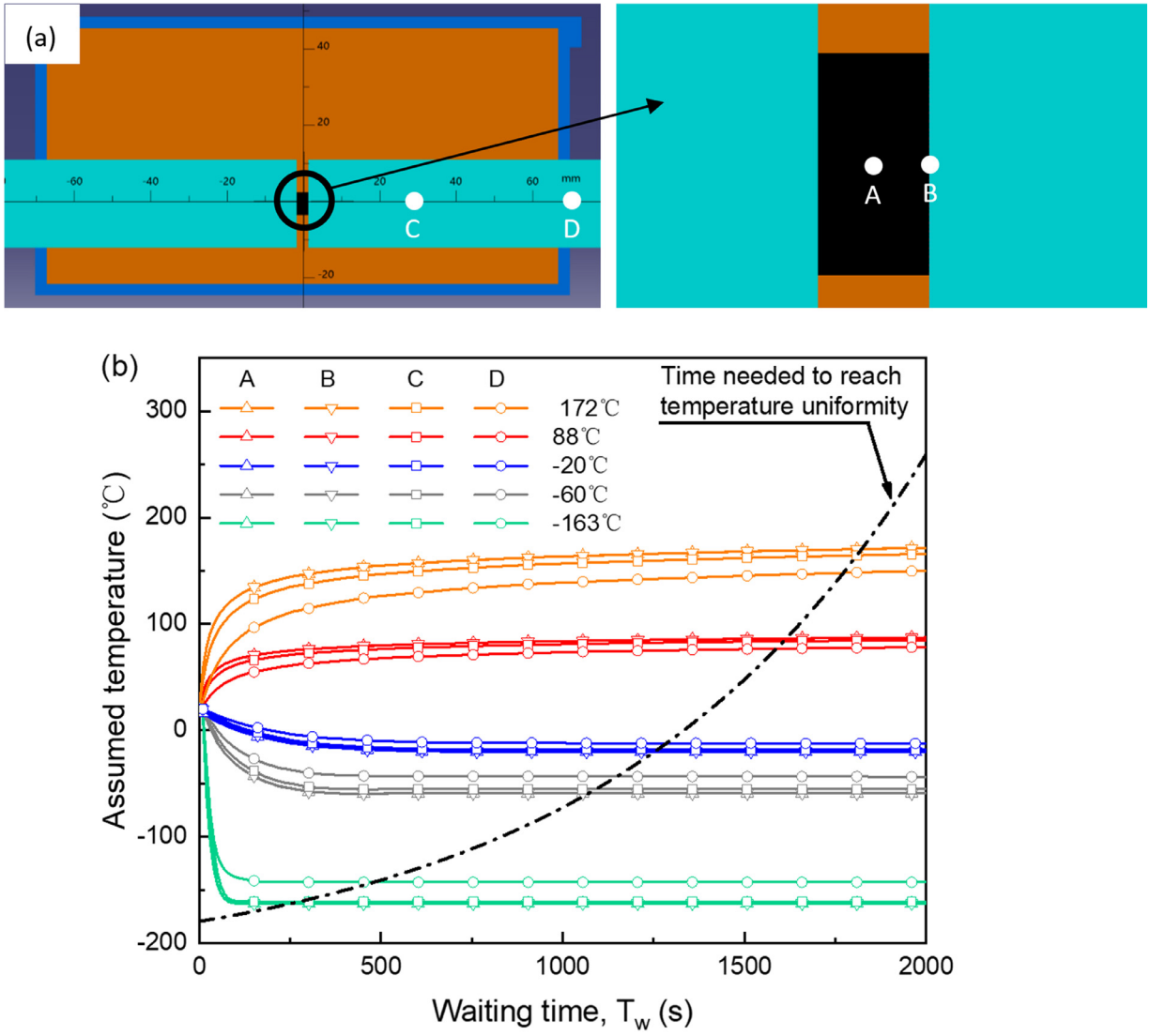


Fig. 8. (a) Positions of temperature measurement and (b) temperature evolution of the four positions.

equilibrium state is achieved from the very beginning of the test and maintains up to the maximum strain. The verified dynamic force equilibrium condition ensures that the experimentally measured stress-strain relations give an accurate deformation behavior description of 304 ASS.

4.2. *True stress-true strain relations of 304 ASS*

The true stress-true strain curves of 304 ASS at temperatures between −163°C and 172°C and strain rates from 10^{-3} s^{-1} to 3270 s^{-1} are shown in Fig. 11. It is seen that for all the tested strain rates and temperatures, the flow stress increases continuously with increasing strain but the strain hardening rates differ. In quasi-static tests (10^{-3} s^{-1} to 1 s^{-1}) conducted at 172°C, the strain hardening rate decreases slowly with increasing strain; as the testing temperature decreases to 88°C, the flow stress increases almost linearly with a constant strain hardening rate; with further decrease of testing temperature, the stress-strain curves exhibit an S-shape and a second hardening phenomenon. As discussed in the introduction section, this phenomenon is also observed by several other authors [14,17,26,27] in TRIP steels and is attributed to the SIMT effect. For temperatures below M_d, which is 140°C for the 304 ASS, martensitic transformation can be triggered by plastic deformation. A mixture of martensite and austenite phases is much harder than pure austenite phase. Therefore, the strain hardening rate is enhanced. At 172°C, a temperature above M_d, the deformation mechanism changes into dislocation glide: the strain hardening rate is controlled by a competition between dislocation generation, accumulation and annihilation [8]. As is pointed out by the unified constitutive model proposed by Lin et al. [8], the dislocations generate and accumulate quickly at small strains, and then the increasing rate of dislocation density decreases gradually at large strains. Therefore, small strain hardening rate at large strains is observed. Concerning dynamic tests (1550 s^{-1} to 3270 s^{-1}) at various testing temperatures, the results are shown in Fig. 11(e), (f) and (g). It is seen that the second hardening phenomenon is not obvious anymore as martensitic transformation is strongly inhibited by the adiabatic heating effect.

4.3. *Strain rate sensitivity of 304 ASS*

The variations of flow stress with strain rate as a function of testing temperature for true strains of 0.05 and 0.2 are plotted in Fig. 12(a) and (b), respectively. They represent respectively the deformation behavior of pure austenite phase and a mixture of austenite and martensite phases.

As shown in Fig. 12(a), the variation of flow stress with strain rate at a true strain of 0.05 is consistent with metallic materials deformed by dislocation glide: the flow stress first remains constant in quasi-static

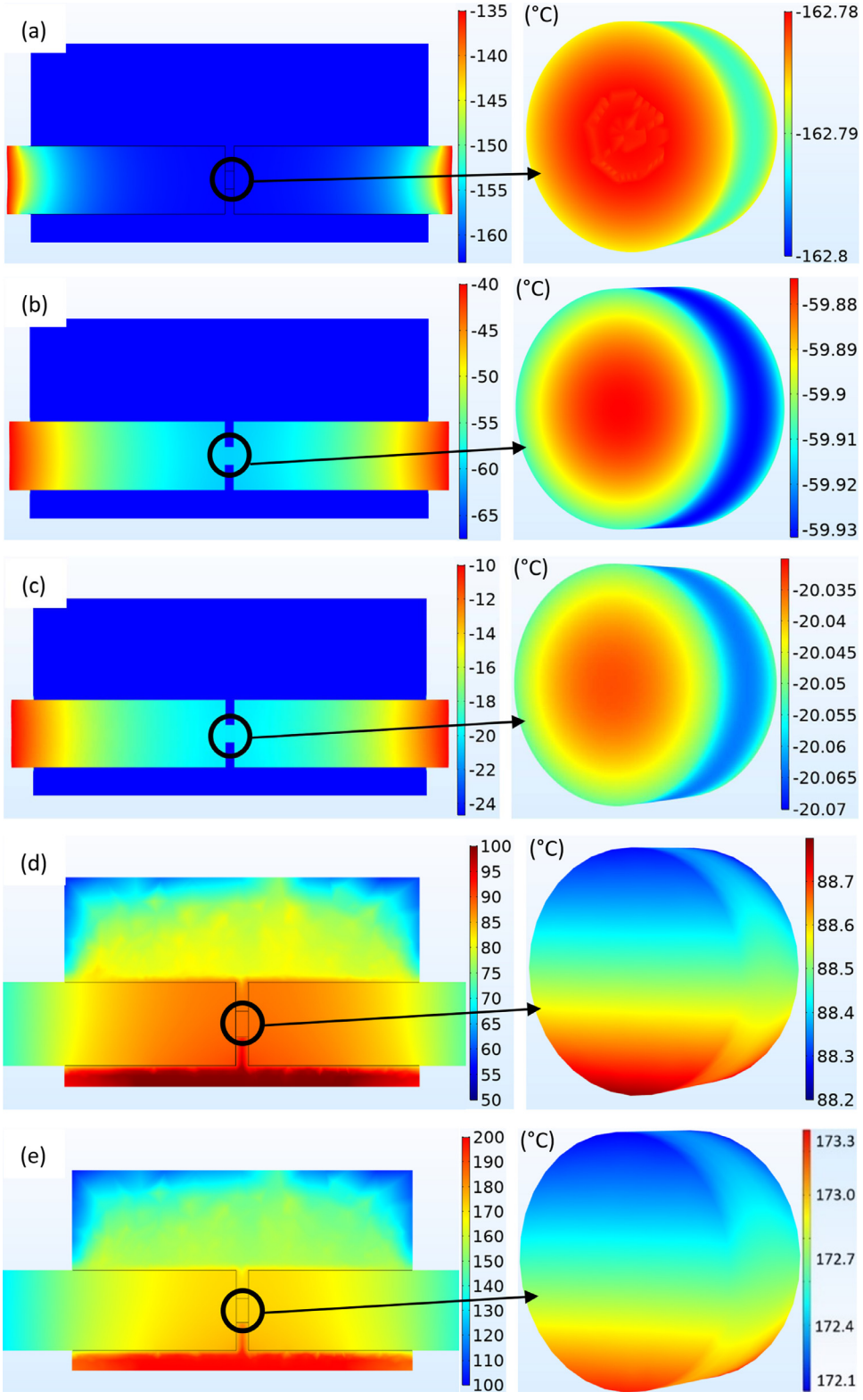


Fig. 9. Temperature distribution in the heating furnace/cooling device with the specimen temperatures stable at: (a) −163°C, (b) −60°C, (c) −20°C, (d) 88°C and (e) 172°C.

tests (10^{-3} s^{-1} to 1 s^{-1}) and then increases continuously in dynamic tests (1550 s^{-1} to 3270 s^{-1}). A phenomenon should be noticed: in dynamic strain rate regime, the strain rate sensitivity is coupled with temperature. The flow stress increases more slowly at low temperatures than that at high temperatures. For thermo-viscoplastic behavior modeling, an item describing the coupling relationship between strain rate and temperature such as the Arrhenius equation is needed.

The evolution of flow stress with strain rate at a true strain of 0.2 is shown in Fig. 12(b). In quasi-static strain rates, the strain rate sensitivity is different from that at the true strain of 0.05. For temperatures below −20°C, the flow stress decreases with increasing strain rate, indicating a negative strain rate sensitivity. In particular, at −163°C, the flow stress in quasi-static tests is even higher than that under dynamic tests. For temperatures above 20°C, the flow stress does not change obviously

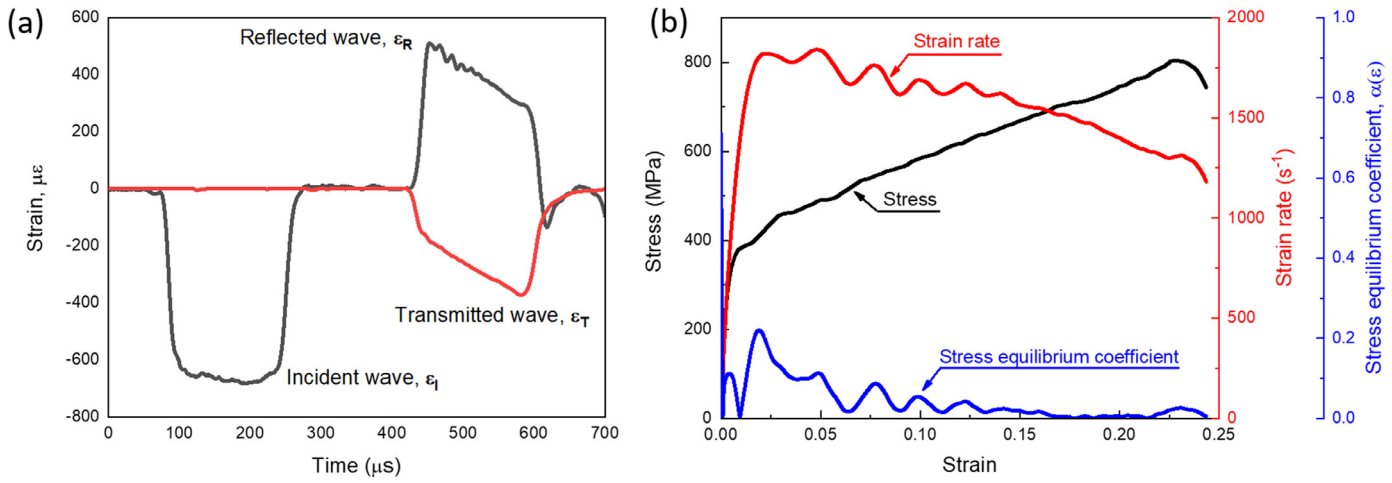


Fig. 10. A typical compression test at 1564 s^{-1} and 172°C: (a) the wave signals and (b) the true stress, strain rate and force equilibrium coefficient vs true strain curves.

with increasing strain rate. In dynamic strain rates, a positive strain rate sensitivity similar to that at the true strain of 0.05 is observed. But the strain rate sensitivity is more pronounced at low temperatures instead of the previously observed high temperatures.

4.4. *Temperature sensitivity of 304 ASS*

Fig. 13 shows the evolution of flow stress with temperature at different strain rates and two strains. As shown in Fig. 13(a), the flow stress decreases with increasing temperature. The decreasing tendencies are around 1.40 MPa/ °C and 1.74 MPa/ °C for quasi-static and dynamic strain rates, respectively. However, from −60°C to −163°C, the dynamic flow stress increases by merely 20 MPa: the strong temperature sensitivity disappears. A similar phenomenon has been observed in HSLA-65 steel by Nemat-Nasser and Guo [28] when the compression behavior was studied over a wide range of strain rates and temperatures. According to the thermally activated dislocation motion theory [29], the total flow stress can be divided into two items called the internal stress σ_μ and the effective stress σ^*. The two parts describe respectively the strain hardening effect and the thermal activation process, Fig. 14. σ_μ is independent of strain rate and keeps almost constant at different temperatures, while σ^* is strongly affected by the effects of strain rate and temperature. During quasi-static (10^{-3} s^{-1} to 1 s^{-1}) tests at various temperatures, σ^* first remains constant and then increases significantly at temperatures lower than $0.1T_m$ (T_m refers to the melting temperature of alloys and is 1300°C for 304 ASS). Hence, from −60°C (0.13 T_m) to −163°C (0.06 T_m), the flow stress increases with decreasing temperature. When the strain rate changes from quasi-static to dynamic (1550 s^{-1} to 3270 s^{-1}), σ^* increases continuously but the stress difference between various temperatures becomes smaller. Therefore, the previous observed strong temperature sensitivity almost vanishes in dynamic tests.

Fig. 13(b) shows the evolution of flow stress with temperature at a true strain of 0.2. Under the effects of strain rate on both the transformation process and the dislocation motion, the flow stress decreases with increasing temperature but the decreasing tendencies in quasi-static and dynamic tests are different: the flow stress decreases faster in the former condition than in the latter.

5. Thermo-viscoplastic behavior modeling of 304 ASS

Motivated by scientific and engineering demands, a large number of constitutive models have been proposed to describe the deformation behavior of materials. Basically, they can be divided into two categories: the phenomenological and the physical based models. The first category describes flow stress of materials according to empirical observations and does not have any physical background, e.g., Johnson-Cook model [31], Khan–Huang model [32], Fields–Backofen model [33], Molinari–Ravichandran model [34], Voce–Kocks model [35], Arrhenius equation [36] and their variants [37–40]. Another group of constitutive models are built according to deformation mechanism of materials, such as Zerilli and Armstrong model [41], Rusinek–Klepaczko model [20], Voyiadjis–Almasri model [42] and Bodner–Partom model [43]. In addition, artificial neural network models are increasingly used in areas of constitutive behavior prediction as they provide a completely different approach to materials modeling than the traditional statistical or numerical methods [44]. A detailed description of different kinds of constitutive models with their advantages and disadvantages can be found in [45].

According to the deformation behavior analysis of 304 ASS in Section 4, a coupling effect of strain rate and temperature exists. Moreover, the deformation behavior is strongly affected by martensitic transformation. Therefore, a constitutive model taking the two effects into consideration is needed for accurate deformation behavior modeling. In this section, an extension of the original RK model considering martensitic transformation [21] is used to describe the deformation behavior of 304 ASS.

A typical true stress-true strain curve of 304 ASS at −20°C and 10^{-3} s^{-1} is shown in Fig. 15. The curve is divided into two parts: within a true strain of 0.08, no martensitic transformation occurs during the deformation process; for larger strains, the deformation mechanism changes into a competition between dislocation slip and martensitic transformation. The true stress-true strain curve without phase transformation can be extended by the same strain hardening rate. The extended curve is assumed as the flow stress of 304 ASS without martensitic transformation and can be described by the original RK model. The difference between the real and the extended stress-strain curve is supposed to be caused by martensitic transformation. The corresponding flow stress can be described by an extended item coupled to the original RK model.

The item defining martensitic transformation is based on the probability that the austenite phase will transform into martensite phase under certain conditions. No accurate phase fraction measurement is needed to define the model parameters. Various martensite fraction measurement techniques can be used but each of them has the limitations and it is pretty difficult to obtain accurate proportions of each phase:

- Metallographic observation is convenient but the results are strongly affected by sample surface preparation techniques.

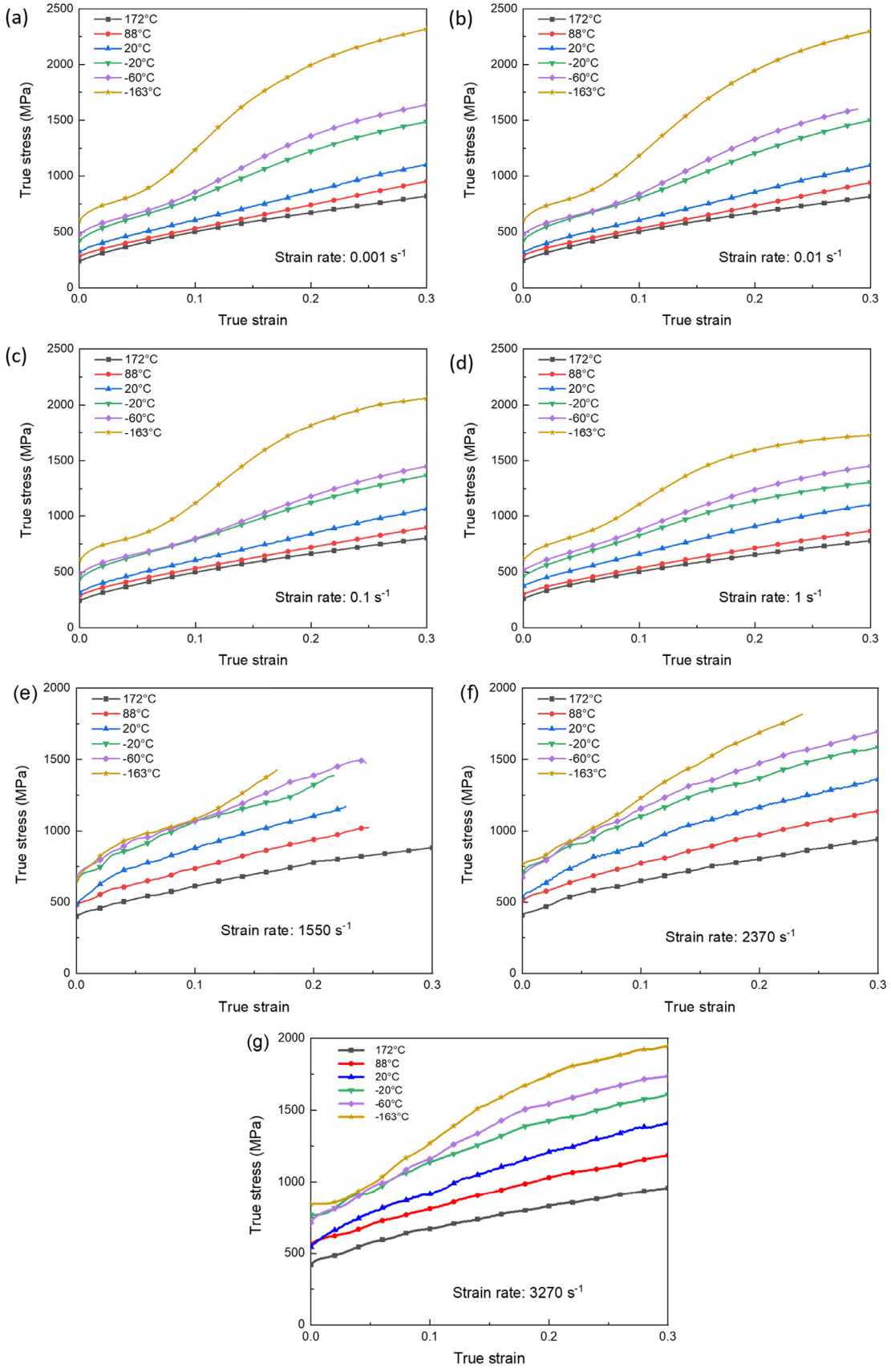


Fig. 11. True stress-true strain relations of 304 ASS as a function of temperature at strain rates of: (a) 10^{-3} s^{-1}, (b) 10^{-2} s^{-1}, (c) 10^{-1} s^{-1}, (d) 1 s^{-1}, (e) 1550 s^{-1}, (f) 2370 s^{-1} and (g) 3270 s^{-1}.

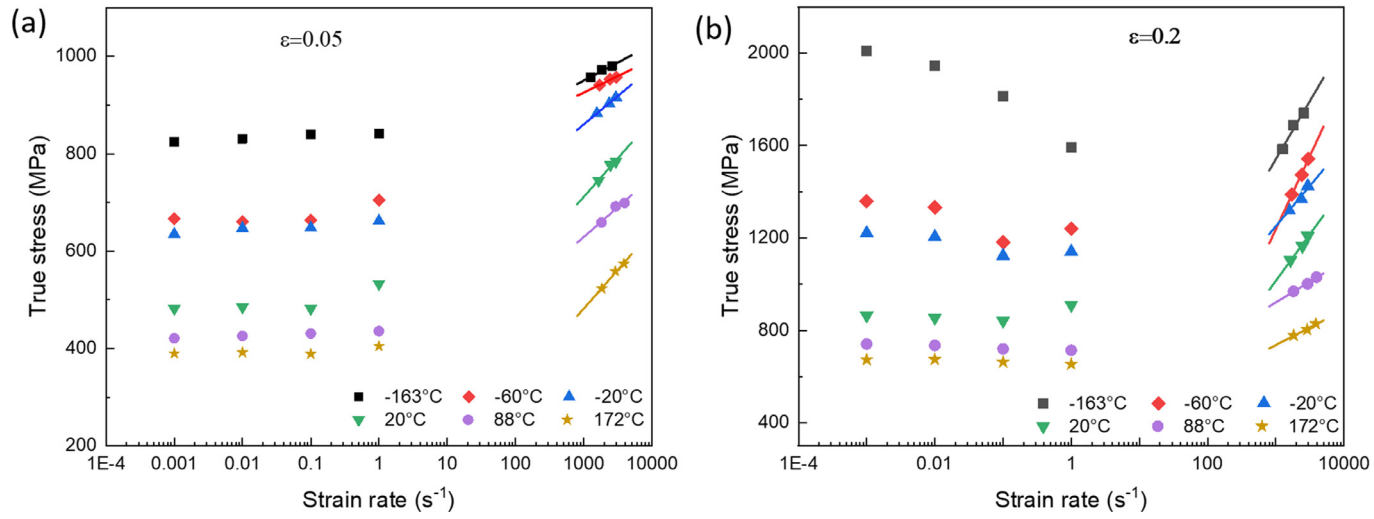


Fig. 12. Variation of flow stress with strain rate as a function of temperature for true strains of: (a) 0.05 and (b) 0.2.

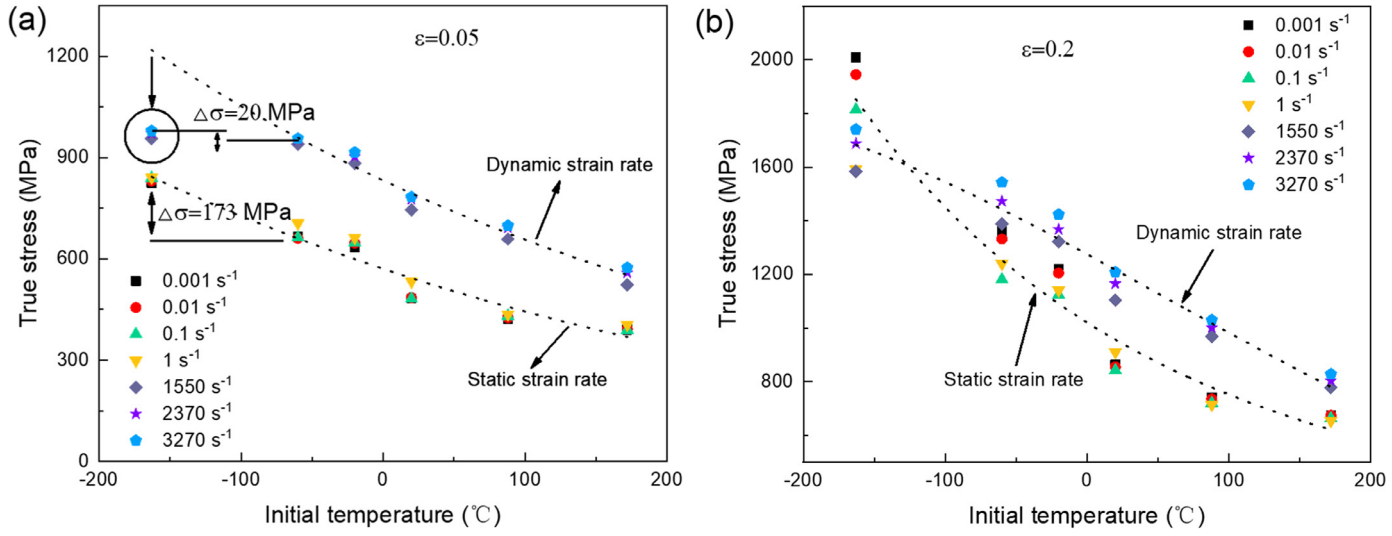


Fig. 13. Variation of flow stress with temperature as a function of strain rate for true strains of: (a) 0.05 and (b) 0.2.

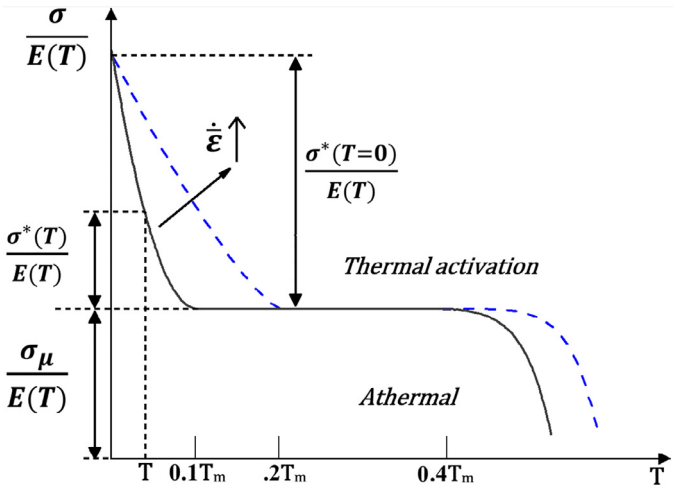


Fig. 14. Decomposition of the total flow stress into the internal stress σ_μ and the effective stress σ^* using the thermally activated dislocation motion theory [30].

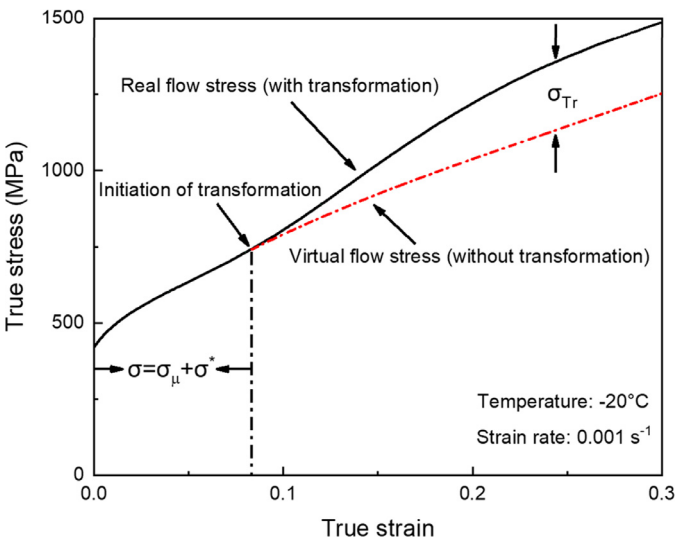


Fig. 15. The true stress-true strain curve of 304 ASS at −20°C and 10^{-3} s^{-1}.

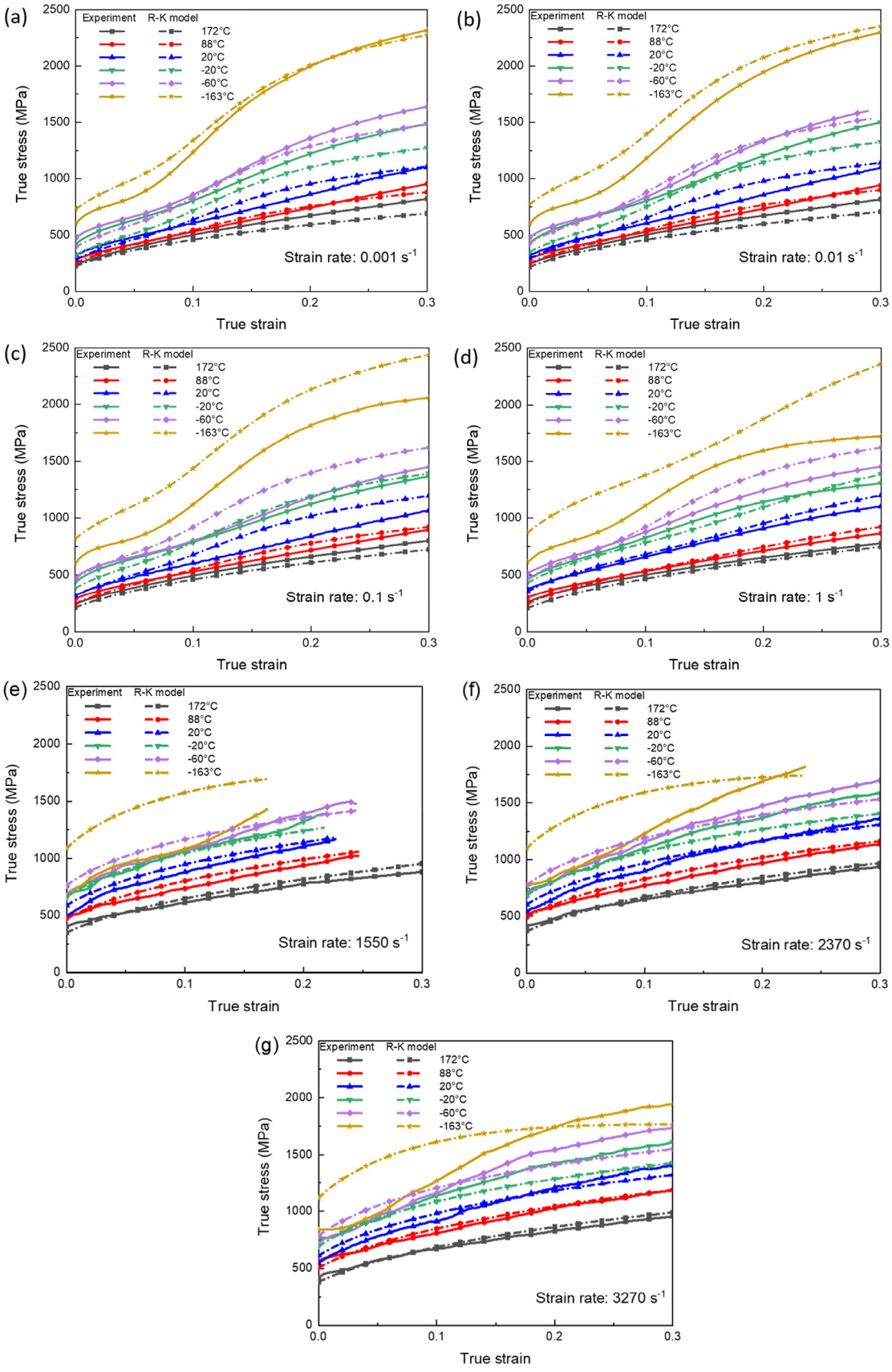


Fig. 16. Comparison of flow stress curves between experiments and RK model for (a) 10^{-3} s^{-1}, (b) 10^{-2} s^{-1}, (c) 10^{-1} s^{-1}, (d) 1 s^{-1}, (e) 1550 s^{-1}, (f) 2370 s^{-1} and (g) 3270 s^{-1}.

- For EBSD, the severe plastic deformation makes the indexing rate decrease a lot, so the measurement results are representative only under small strains.
- The detection area of XRD is limited to the sample surface.
- Magnetic permeability measurement is also used to calculate martensite fraction but the inverse magnetostriction phenomenon cannot be avoided.

Without martensite fraction measurement, the error caused by inaccurate measurement methods can be largely avoided.

5.1. The extended R-K constitutive equation

Inspired by the thermally-activated dislocation motion theory [29], the original form of the RK model is given as a sum of two components: the internal stress $\sigma_\mu(\bar{\varepsilon}^p, \dot{\bar{\varepsilon}}^p, T)$ and the effective stress $\sigma^*(\dot{\bar{\varepsilon}}^p, T)$, Fig. 14. The former component is induced by long-range barriers to dislocation motion and is independent of deformation conditions. In contrast, the latter component is caused by short-range barriers to dislocation motion such as the interactions of dislocations and crystal defects, and can be overcome by thermal activation process [13]. The two components are multiplied by a parameter $E(T)/E_0$ to represent the temperature dependence of Young's modulus.

$$\bar{\sigma}\left(\bar{\varepsilon}^p, \dot{\bar{\varepsilon}}^p, T\right) = \frac{E(T)}{E_0}\left[\left(\bar{\varepsilon}^p, \dot{\bar{\varepsilon}}^p, T\right) + \sigma^*\left(\dot{\bar{\varepsilon}}^p, T\right)\right] \tag{4}$$

A strain hardening equation similar to the Swift law is used to describe the internal stress $\sigma_\mu(\bar{\varepsilon}^p, \dot{\bar{\varepsilon}}^p, T)$.

$$\sigma_\mu\left(\bar{\varepsilon}^p, \dot{\bar{\varepsilon}}^p, T\right) = B\left(\dot{\bar{\varepsilon}}^p, T\right)\left(\varepsilon_0 + \bar{\varepsilon}^p\right)^{n\left(\dot{\bar{\varepsilon}}^p, T\right)} \tag{5}$$

where ε_0 refers to the value corresponding to the yield point during quasi-static tests.

The effective stress $\sigma^*(\dot{\bar{\varepsilon}}^p, T)$ defines the flow stress induced by thermal activation process using an Arrhenius equation:

$$\sigma^*\left(\dot{\bar{\varepsilon}}^p, T\right) = {\sigma^*}_0\left\langle 1 - D_1\left(\frac{T}{T_m}\right)\log\log\left(\frac{\dot{\varepsilon}_{\max}}{\dot{\bar{\varepsilon}}p}\right)\right\rangle^{m^*} \tag{6}$$

where σ_0^* is the effective stress at 0 K, D_1 and m^* are material constants.

To define the stress component caused by martensitic transformation, a third item $\sigma_{Tr}(\bar{\varepsilon}^p, \dot{\bar{\varepsilon}}^p, T)$ is coupled to the original R-K model.

$$\bar{\sigma}\left(\bar{\varepsilon}^p, \dot{\bar{\varepsilon}}^p, T\right) = \frac{E(T)}{E_0}\left[\sigma_\mu\left(\bar{\varepsilon}^p, \dot{\bar{\varepsilon}}^p, T\right) + \sigma^*\left(\dot{\bar{\varepsilon}}^p, T\right)\right] + \sigma_{Tr}\left(\bar{\varepsilon}^p, \dot{\bar{\varepsilon}}^p, T\right) \tag{7}$$

$$\sigma_{Tr}\left(\bar{\varepsilon}^p, \dot{\bar{\varepsilon}}^p, T\right) = \sigma_0^\alpha f\left(\bar{\varepsilon}^p, \dot{\bar{\varepsilon}}^p\right) g(T) \tag{8}$$

where σ_0^α refers to the maximum stress increase caused by martensitic transformation. The value should be obtained by mechanical tests at the lowest temperature of interest.

$f(\bar{\varepsilon}^p, \dot{\bar{\varepsilon}}^p)$ is a phenomenological function to describe the effects of strain rate and strain on the probability of martensitic transformation. It is given as

$$f\left(\bar{\varepsilon}^p, \dot{\bar{\varepsilon}}^p\right) = \left[1 - exp\left(-h\left(\dot{\bar{\varepsilon}}^p\right)\bar{\varepsilon}^p\right)\right]^\xi \tag{9}$$

$$h\left(\dot{\bar{\varepsilon}}^p\right) = \lambda_0 \exp\left(-\lambda\dot{\bar{\varepsilon}}^p\right) \tag{10}$$

where ξ is a constant that defines the strain value for which the austenite phase starts to transform into martensite phase. The value can be determined according to the interrupt increase in strain hardening rate of stress-strain curves. $h(\dot{\bar{\varepsilon}}^p)$ is a function that describes the strain rate dependent martensitic transformation. λ_0 and λ are two shape fitting parameters. A detailed description concerning the fitting results of phase transformation using $h(\dot{\bar{\varepsilon}}^p)$ can be found in [21].

To define the effect of temperature on the transformation process, a temperature function $g(T)$ is proposed:

$$g(T) = 1 - \left(\frac{T - M_S}{M_D - M_S}\right)^n \tag{11}$$

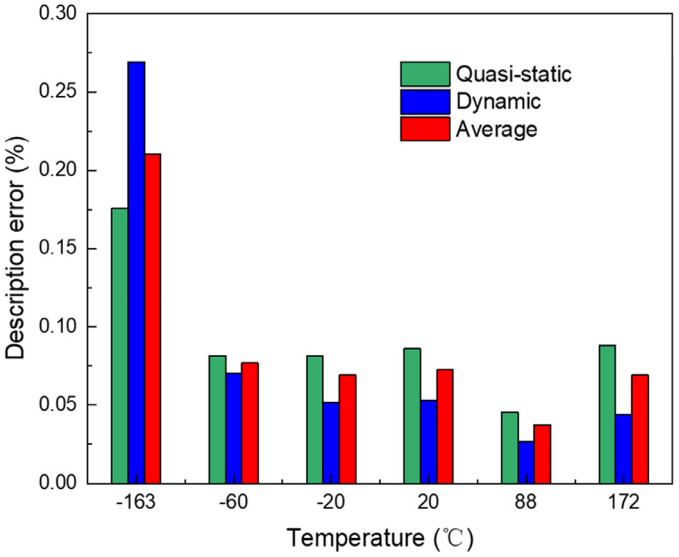


Fig. 17. The description error of the extended R-K model in prediction of the experimental data.

where M_S refers to the temperature below which the Gibbs free energy between austenite phase and martensite phase is high enough for martensitic transformation to occur spontaneously. M_D is the temperature above which martensitic transformation does not occur anymore and the deformation mechanism changes into twinning or dislocation slip. n represents the strain rate sensitivity of the transformation process.

The determination of extended RK model parameters is divided into two steps: first of all, the extended curves of 304 ASS under different strain rates and temperatures are regarded as the stress-strain relations without martensitic transformation and are then defined by the original RK model. A detailed description of the fitting procedures can be found in [30]. After that, the stress component caused by martensitic transformation is defined by the third item σ_{Tr} of the extended RK model. In both steps, a least square method is used to minimize the error between the calculated data and the experimental results.

The total number of material constants of the extended RK model is 12 including 4 parameters to define martensitic transformation. The fitted material parameters of the original R-K model and the extended item are shown in Tables 2 and 3, respectively.

5.2. Comparison between experimental and predicted flow stress of 304 ASS

A comparison between experiments and predicted stress-strain curves as well as the corresponding prediction errors are shown in Figs. 16 and 17, respectively. The prediction error Δ is used to assess the fitting results and is defined as

$$\Delta = \frac{1}{N}\sum_{i=1}^{N}\left|\frac{\sigma_i^{exp} - \sigma_i^{pre}}{\sigma_i^{exp}} \times 100\%\right| \tag{12}$$

It is seen from Figs. 16 and 17 that a good agreement is achieved for testing temperatures between −60°C and 172°C. The prediction errors are respectively 7.6% and 4.9% for quasi-static and dynamic tests. According to J.A.Rodríguez-Martínez et al. [46], an obvious temperature increase still exists in quasi-static tests of TRIP steels, and it affects martensitic transformation significantly. However, in this study, the quasi-static tests are considered as isothermal. Therefore, the predicted results for quasi-static tests are not as good as the dynamic ones. In addition, due to the unexpected low strain rate sensitivity of 304 ASS at −163°C, Fig. 13, the predicted flow stress is significantly higher than the experimental ones with an average error of 21.2%.

Table 2
The fitted parameters of the original RK model for 304 ASS without martensitic transformation.

E_0 (GPa)	T_m (K)	θ^* (-)	σ_0^* (MPa)	D_1 (-)	m^* (-)	B_0 (MPa)	ν (-)	n_0 (-)	D_2 (-)	ε_0 (-)
210	1700	0.9	658	0.58	1.84	1693	0.41	0.39	−0.19	0.023

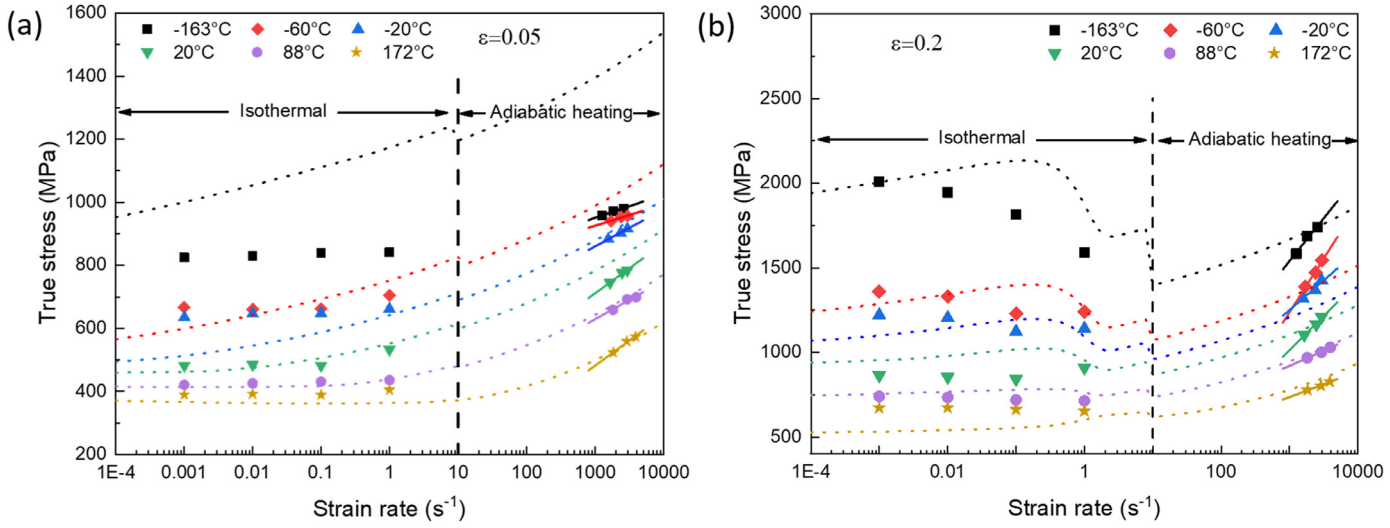


Fig. 18. Comparison of strain rate sensitivity between experiments and the extended RK model at true strains of (a) 0.05 and (b) 0.2.

Table 3
The fitted parameters of the extended item describing the martensitic transformation.

σ_0 (MPa)	M_D (K)	M_S (K)	λ (-)	λ_0 (-)	ξ (-)	η (-)
1026	413	20	0.60	21.17	10.76	0.82

This is mainly because in the extended RK model, a phenomenological instead of physical function is used to describe the martensitic transformation process. The function works well within a limited temperature regime. Compared to sophisticated physical models [47–49], the phenomenological approach simplifies the finite element (FE) code implementation process and helps to reduce the computational time. However, for a better martensitic transformation behavior description, a further improvement of the extended RK model is needed.

To compare the experimental data with the predicted ones in detail, the evolution of flow stress with strain rate for two strains 0.05 and 0.2 are shown in Fig. 18. It is clear in Fig. 18(a) that the extended RK model gives a satisfactory prediction of strain rate sensitivity at various temperatures, except −163°C. In dynamic strain rates, the coupling relationship between strain rate and temperature is also captured: the material shows higher strain rate sensitivity at elevated temperatures. In Fig. 18(b), the negative strain rate sensitivity in quasi-static strain rates is not predicted correctly. As explained before, this is because in quasi-static tests, the experimentally observed temperature rise is not taken into consideration when performing constitutive behavior modeling.

Concerning predictions of temperature sensitivity, a comparison between experiments and the extended RK model is shown in Fig. 19. It is clear that the model defines the temperature sensitivity accurately between −60°C and 172°C. In Fig. 19(b), the decreased temperature sensitivity with increasing strain rate is also captured. On the whole, the extended R-K model predicts the deformation behavior of 304 ASS correctly for testing temperatures $T_0 \geqq -60°C$.

6. Validation of the extended RK model

The utility of a constitutive model lies in not only its capacity of fitting experimentally obtained results but also its ability to predict deformation behavior beyond the testing conditions. To evaluate the extended RK model and the previously defined model parameters, numerical simulations of 304 ASS plates impacted by a conical projectile at different temperatures have been carried out.

6.1. Numerical model description

The numerical simulations were performed based on the ballistic impact results of 304 ASS reported by Jia et al. [24]. During experiments, 304 ASS thin plates were impacted by a conical projectile under sub-ordnance velocities ranging from 80 m/s to 180 m/s and initial temperatures between −60°C and 200°C. Each plate is a square with a side length of 130 mm and a thickness of 1.5 mm. The conical projectile is a cylinder with a diameter of 12.8 mm and a height of 25 mm. At the top of the projectile, a conical nose with an angle of 72° is machined. A detailed description of the ballistic impact set-up, the conical projectile and the cooling device/heating furnace for low/elevated temperature tests can be found in [24].

A 3D full-size finite element (FE) model consisting of the projectile and the target has been built using software ABAQUS/Explicit, Fig. 20. The geometry and dimensions of the target are exactly the same as the experimental ones. The target is set as a deformable body, and the constitutive behavior is characterized by the previously defined extended RK model. To reduce calculation time, the projectile is regarded as a rigid body with a constant mass of 29 g. The four edges of the target are fixed and no displacement is allowed. The conical projectile is placed perpendicular to the target with a predefined velocity. For contact between the projectile and the target, penalty method with a friction coefficient of 0.1 is adopted, a value frequently used for dry steel-steel contact [50]. The perforation process is assumed as adiabatic, no heat transfer between the target and the projectile or the surrounding environment is taken into consideration.

According to a mesh convergence study, the optimal mesh density distribution in the target is shown in Fig. 21. The central part of the target is built with 107380 C3D8R elements (8-node linear brick, reduced integration element) with an initial element size of 0.2 mm. ALE adaptive meshing is used to maintain a high mesh quality throughout the analysis. In the exterior area, where no projectile/target impact occurs,

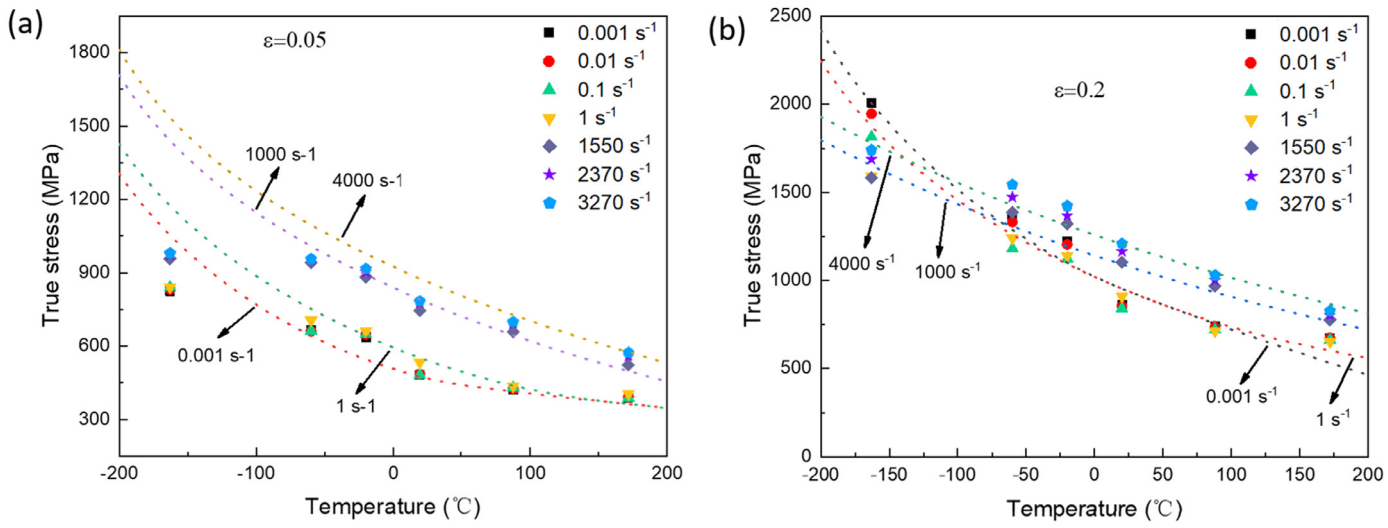


Fig. 19. Comparison of temperature sensitivity between experiments and the extended RK model at true strains of: (a) 0.05 and (b) 0.2.

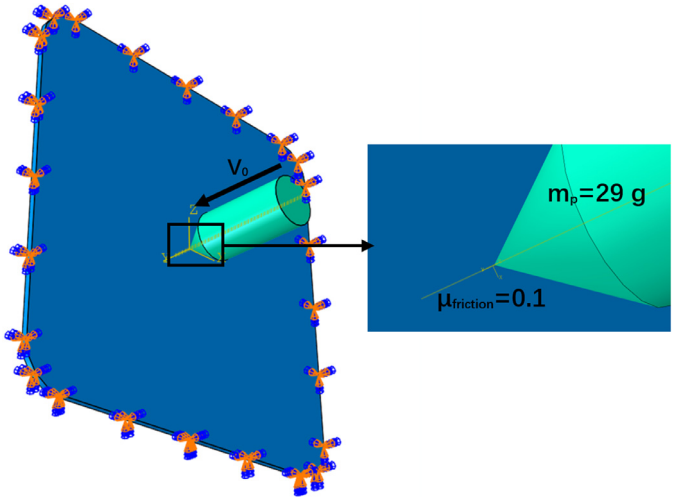


Fig. 20. The finite element model of ballistic impact tests.

Table 4
Failure strains of 304 ASS plate for different testing temperatures.

Initial temperature (℃)	−60	−20	20	200
Failure strain, ε_f	0.49	0.55	0.6	0.67

C3D8R elements with an initial element size of 1.5 mm are adopted. In the whole target, five elements across the thickness direction are used. This mesh density is recommended by several authors when modeling ballistic impact behavior of thin metallic structures [50,51].

To be able to capture the fracture process, a failure criterion with element deletion is necessary. According to the work of Kpenyigba et al. [51], a constant failure strain for each projectile shape is able to produce numerical results in a good agreement with experiments. In this work, a constant failure strain is assumed for each testing temperature. According to an optimization of ballistic curves, the failure strains for different testing temperatures were estimated, Table 4.

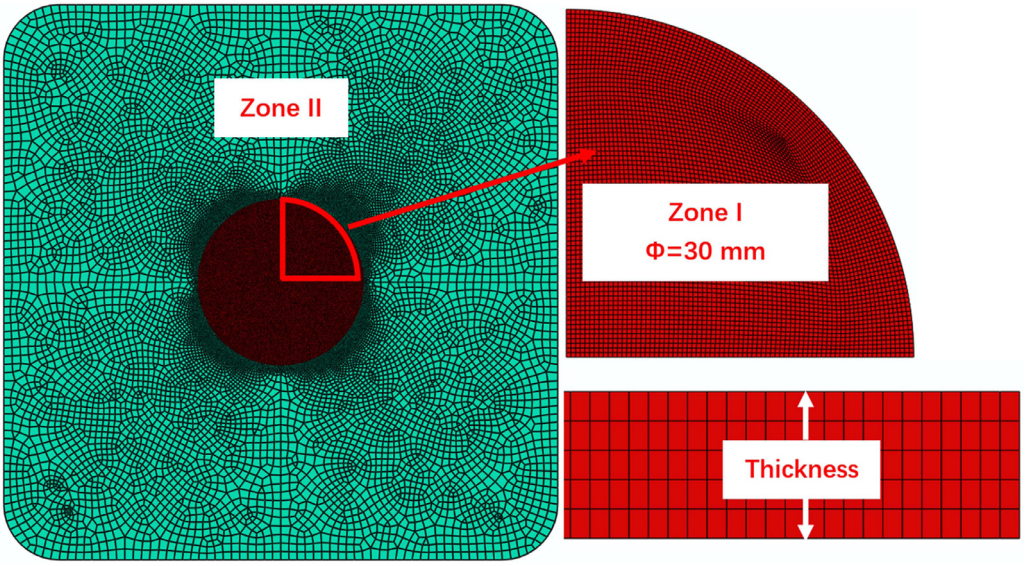


Fig. 21. Mesh density distribution in numerical simulations.

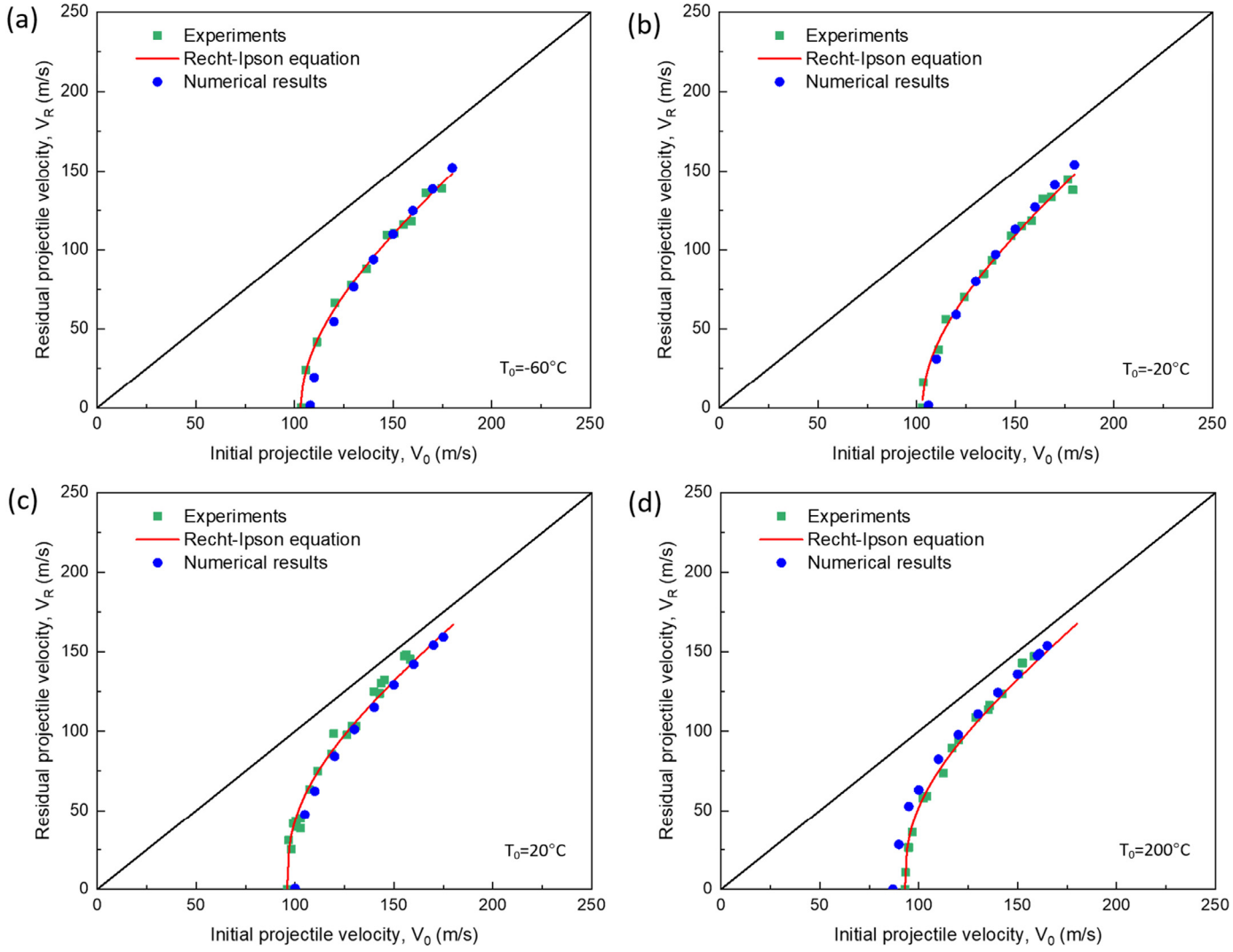


Fig. 22. Comparison of ballistic curves between experiments and numerical simulations: (a) −60°C, (b) −20°C, (c) 20°C and (d) 200°C.

6.2. *Numerical results in terms of ballistic curves and fracture patterns*

The experimental results in terms of ballistic curves V_R-V_0 are presented in Fig. 22. The curves are then fitted to the equation proposed by Recht and Ipson [52], Eq. (13). In Eq. (13), the residual velocity of the projectile V_R is calculated as a function of the initial velocity V_0, the ballistic limit velocity V_{bl} and a fitting parameter α.

$$V_R = \left(V_0{}^{\alpha} - V_{bl}{}^{\alpha}\right)^{1/\alpha} \tag{13}$$

A comparison between the experimental and the numerical ballistic curves is shown in Fig. 22. A good agreement is observed for all the four temperatures. With the increasing testing temperature from −60°C to −20°C, 20°C and 200°C, the predicted ballistic limit velocities decrease gradually from 108 m/s to 106 m/s, 100 m/s and 87 m/s. The prediction errors of V_{bl} for the four temperatures are respectively 4.9%, 2.9%, 4.2% and 6.5%. In addition, the evolution tendency of V_R with V_0 is also captured correctly by numerical simulations. Under all the four temperatures, the V_R-V_0 curves show a parabolic shape. Fitting the numerical V_R-V_0 curves into Eq. 16, the fitted values of parameter α for different temperatures are shown in Table 5. It is seen that in both experiments and numerical simulations, values of α increase with increasing testing temperature, indicating a deteriorated ballistic impact resistance and a lower ballistic limit velocity at high temperatures. Therefore, the evolutions of V_{bl} and α are consistent with each other.

Table 5
Parameter α under different testing temperatures in both experiments and numerical simulations.

Initial temperature (°C)	−60	−20	20	200
Values of α using experimental V_R-V_0	2.285	2.239	2.713	2.766
Values of α using numerical V_R-V_0	2.028	2.005	2.712	2.660

For a complete validation of the extended RK model, the predicted failure mode is compared to the experimental ones, Fig. 23. It is seen that petalling resulting from radial necking during the piercing process is observed, the same as experiments. Plastic deformation is only observed in petals of the perforated specimens, especially on the fracture surface where the material experienced the largest deformation until failure; plastic deformation in the other parts of the specimens is pretty limited, with a maximum value of 1.1% for different testing temperatures.

The number of petals varies under different testing temperatures. A comparison of the number of petals between experiments and numerical results is shown in Table 6. During numerical simulations, the value decreases continuously from 6 at −60°C to 4 at 200°C. In experiments, a similar tendency is observed but the corresponding values are comparatively smaller. In any case, to have a better understanding of the

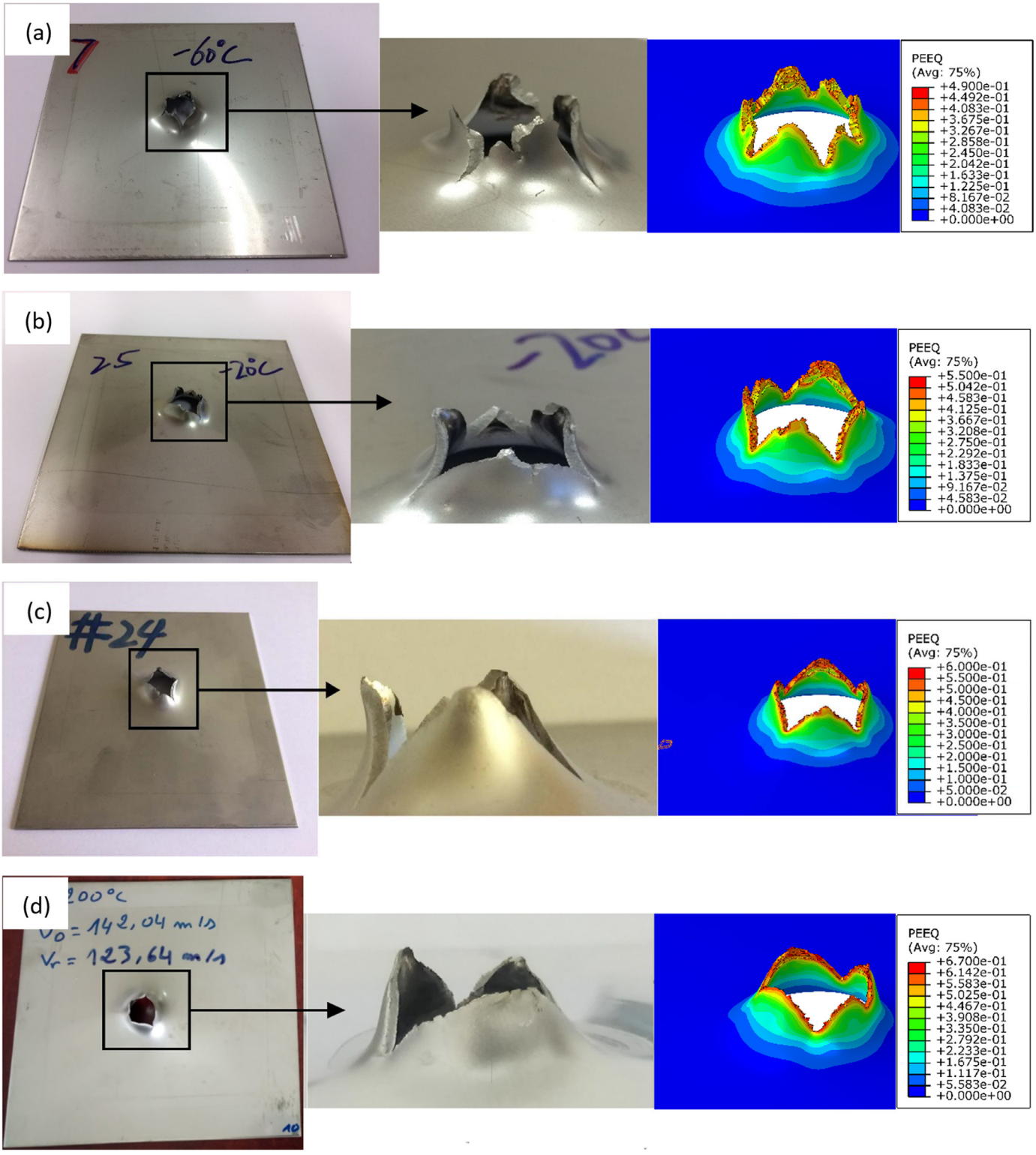


Fig. 23. Comparison of fracture pattern between experiments and numerical simulations: (a) −60°C, (b) −20°C, (c) 20°C and (d) 200°C.

Table 6
Experimental and numerical number of petals as a function of testing temperature at V_0=110 m/s.

Initial temperature (°C)	−60	−20	20	200
Number of petals in experiments	5	4	3	3
Number of petals in numerical simulations	6	5	4	4

failure mode, a further study on the failure behavior of 304 ASS as a function of strain rate, temperature and stress state is necessary.

7. Conclusions and remarks

The thermo-viscoplastic behavior of 304 ASS has been systematically studied over a wide range of strain rates (10^{-3} s^{-1} to 3270 s^{-1}) and

temperatures (−163˚C to 172˚C). Dynamic tests at low/elevated temperatures were conducted using the Hopkinson technique coupled with specifically designed cooling device/heating furnace, and reliability of the technique was verified by thermal simulations. The deformation behavior of 304 ASS was analyzed in terms of strain hardening rate, strain rate sensitivity and temperature sensitivity. Based on experimental results, an extension of the RK model considering SIMT effect was used to describe the constitutive behavior of 304 ASS. The correctness of the extended RK model was further verified through numerical simulations of ballistic impact tests at various testing temperatures. Several noteworthy conclusions are drawn:

1 With the developed cooling device/heating furnace, dynamic tests at temperatures ranging from −163˚C to 172˚C can be conducted using the Hopkinson technique. According to the numerical results, the temperature distribution within the compression specimen is uniform with a maximum fluctuation of 1.2˚C.
2 The deformation behavior of 304 ASS is dominated by a competition between dislocation glide and martensitic transformation. Both strain rate and temperature have significant effects on the two mechanisms. Hence, the deformation behavior of 304 ASS, mainly represented by the strain hardening rate, strain rate sensitivity and temperature sensitivity, is different from metallic alloys commonly deformed by dislocation slip. Several unexpected phenomena such as the S-shaped stress-strain curves, the negative strain rate sensitivity and the changing temperature sensitivity from quasi-static to dynamic strain rates, are observed.
3 From −60˚C to −163˚C and under dynamic strain rates, the temperature sensitivity of 304 ASS was lower than that for the other temperatures. According to the thermally activated dislocation motion theory, this is mainly caused by the comparatively smaller effective stress σ^* increase from −60˚C to −163˚C.
4 The extended RK model was used to describe the constitutive behavior of 304 ASS with an additional item linked to martensitic transformation. The model predicted the flow stress curves of 304 ASS above −60˚C correctly with the several unexpected phenomena being captured. The prediction errors for quasi-static and dynamic tests were 7.6% and 4.9%, respectively.
5 The utility of the extended RK model was further evaluated by numerical simulations of ballistic impact tests at various temperatures between −60˚C and 200˚C. The numerical results in terms of ballistic curves were compared to experiments: both the ballistic limit velocities V_{bl} and the ballistic curves V_R-V_0 were predicted accurately. In addition, the failure process was also captured: both the failure pattern and the number of petals under different temperatures were predicted correctly.

Author statement

The idea and structure of the article were proposed by Alexis Rusinek and Raphaël Pesci. The set-up design and experiments were conducted by Bin Jia, Richard Bernier and Slim Bahi. Bin Jia, Alexis Rusinek and Slim Bahi performed constitutive behavior modeling and numerical simulations of ballistic impact behavior. The paper writing was mainly done by Bin Jia with suggestions and modifications from Alexis Rusinek and Raphaël Pesci. All authors read and approved the final manuscript.

Declaration of Competing Interest

The authors declared that they have no conflicts of interest in this work. We declare that we do not have any commercial or associative interest that represents a conflict of interest in connection with the work submitted.

Acknowledgements

Part of this work was financially supported by the China Scholarship Council under Grant 201606220056.

References

[1] Fischer FD, Sun Q-P, Tanaka K. Transformation-induced plasticity (TRIP). Appl Mech Rev 1996;49:317–64. https://doi.org/10.1115/1.3101930.
[2] Zackay VF, Parker ER, Fahr D, Busch R. The enhancement of ductility in high--strength steels. ASM Trans Quart 1967;60:252–9.
[3] Park WS, Yoo SW, Kim MH, Lee JM. Strain-rate effects on the mechanical behavior of the AISI 300 series of austenitic stainless steel under cryogenic environments. Mater Des 2010;31:3630–40. https://doi.org/10.1016/j.matdes.2010.02.041.
[4] Kumar S, Kwon H-T, Choi K-H, Hyun Cho J, Lim W, Moon I. Current status and future projections of LNG demand and supplies: a global prospective. Energy Policy 2011;39:4097–104. https://doi.org/10.1016/j.enpol.2011.03.067.
[5] Curtze S, Kuokkala V-T, Hokka M, Peura P. Deformation behavior of TRIP and DP steels in tension at different temperatures over a wide range of strain rates. Mater Sci Eng A 2009;507:124–31. https://doi.org/10.1016/j.msea.2008.11.050.
[6] Rodríguez-Martínez JA, Rusinek A, Pesci R. Experimental survey on the behaviour of AISI 304 steel sheets subjected to perforation. Thin-Wall Struct 2010;48:966–78. https://doi.org/10.1016/j.tws.2010.07.005.
[7] Lee W-S, Lin C-F, Chen T-H, Luo W-Z. High temperature deformation and fracture behaviour of 316 L stainless steel under high strain rate loading. J Nucl Mater 2012;420:226–34. https://doi.org/10.1016/j.jnucmat.2011.10.005.
[8] Lin YC, Dong W-Y, Zhou M, Wen D-X, Chen D-D. A unified constitutive model based on dislocation density for an Al-Zn-Mg-Cu alloy at time-variant hot deformation conditions. Mater Sci Eng A 2018;718:165–72. https://doi.org/10.1016/j.msea.2018.01.109.
[9] Byun TS, Hashimoto N, Farrell K. Temperature dependence of strain hardening and plastic instability behaviors in austenitic stainless steels. Acta Mater 2004;52:3889–99. https://doi.org/10.1016/j.actamat.2004.05.003.
[10] Hamada AS, Karjalainen LP, Misra RDK, Talonen J. Contribution of deformation mechanisms to strength and ductility in two Cr–Mn grade austenitic stainless steels. Mater Sci Eng A 2013;559:336–44. https://doi.org/10.1016/j.msea.2012.08.108.
[11] Zheng C, Yu W. Effect of low-temperature on mechanical behavior for an AISI 304 austenitic stainless steel. Mater Sci Eng A 2018;710:359–65. https://doi.org/10.1016/j.msea.2017.11.003.
[12] Krizan D. TRIP steels: advanced high strength multiphase steels for automotive applications. Proc Int Conf 2006:659–68 on “COM-MATTECH”, Trnava, Slovakia.
[13] Lin YC, Yang H, He D-G, Chen J. A physically-based model considering dislocation–solute atom dynamic interactions for a nickel-based superalloy at intermediate temperatures. Mater Des 2019;183:108122. https://doi.org/10.1016/j.matdes.2019.108122.
[14] Talonen J, Hänninen H, Nenonen P, Pape G. Effect of strain rate on the strain-induced $\gamma \rightarrow \alpha'$-martensite transformation and mechanical properties of austenitic stainless steels. Metall Mat Trans A 2005;36:421–32. https://doi.org/10.1007/s11661-005-0313-y.
[15] Lee W-S, Lin C-F. Impact properties and microstructure evolution of 304 L stainless steel. Mater Sci Eng A 2001;308:124–35. https://doi.org/10.1016/S0921-5093(00)02024-4.
[16] Park WS, Chun MS, Han MS, Kim MH, Lee JM. Comparative study on mechanical behavior of low temperature application materials for ships and offshore structures: part I—Experimental investigations. Mater Sci Eng A 2011;528:5790–803. https://doi.org/10.1016/j.msea.2011.04.032.
[17] Lichtenfeld JA, Van Tyne CJ, Mataya MC. Effect of strain rate on stress-strain behavior of alloy 309 and 304 L austenitic stainless steel. Metall Mat Trans A 2006;37:147–61. https://doi.org/10.1007/s11661-006-0160-5.
[18] Ishikawa K, Tanimura S. Strain rate sensitivity of flow stress at low temperatures in 304n stainless steel. Int J Plastic 1992;8:.. 947–58 https://doi.org/10.1016/0749-6419(92)90044-D .
[19] Gür C., Pan J. Handbook of thermal process modelling of steels. 2009. CRC Press: Boca Raton, FL; n.d.
[20] Rusinek A, Klepaczko JR. Shear testing of a sheet steel at wide range of strain rates and a constitutive relation with strain-rate and temperature dependence of the flow stress. Int J Plastic 2001;17:87–115. https://doi.org/10.1016/S0749-6419(00)00020-6.
[21] Rodríguez-Martínez JA, Rusinek A, Klepaczko JR, Pęcherski RB. Extension of R–K constitutive relation to phase transformation phenomena. Mater Des 2009;30:2513–20. https://doi.org/10.1016/j.matdes.2008.09.043.
[22] Malinowski JZ, Klepaczko JR. A unified analytic and numerical approach to specimen behaviour in the Split-Hopkinson pressure bar. Int J Mech Sci 1986;28:381–91. https://doi.org/10.1016/0020-7403(86)90057-3.
[23] Xu Z, Ding X, Zhang W, Huang F. A novel method in dynamic shear testing of bulk materials using the traditional SHPB technique. Int J Impact Eng 2017;101:90–104. https://doi.org/10.1016/j.ijimpeng.2016.11.012.
[24] Jia B., Rusinek A., Bahi S., Bernier R., Pesci R., Bendarma A. Perforation behavior of 304 stainless steel plates at various temperatures. J Dyn Behav Mater2019:1–16. https://doi.org/10.1007/s40870-019-00208-9.
[25] COMSOL A. COMSOL Multiphysics Reference Manual: Version 3.5. Stockholm; 2008.
[26] Murr LE, Staudhammer KP, Hecker SS. Effects of strain state and strain rate on deformation-induced transformation in 304 stainless steel: part II. Microstructural study. MTA 1982;13:627–35. https://doi.org/10.1007/BF02644428.

[27] Hecker SS, Stout MG, Staudhammer KP, Smith JL. Effects of strain state and strain rate on deformation-induced transformation in 304 stainless steel: part I. Magnetic measurements and mechanical behavior. MTA 1982;13:619–26. https://doi.org/10.1007/BF02644427.
[28] Nemat-Nasser S., Guo W.-.G. Mechanics of materials 2005;37:379–405. https://doi.org/10.1016/j.mechmat.2003.08.017.
[29] Kocks UF, Argon AS, Ashby MF. Thermodynamics and kinetics of slip. Argonne National Laboratory; 1973.
[30] Klepaczko JR, Rusinek A, Rodríguez-Martínez JA, Pęcherski RB, Arias A. Modelling of thermo-viscoplastic behaviour of DH-36 and Weldox 460-E structural steels at wide ranges of strain rates and temperatures, comparison of constitutive relations for impact problems. Mech Mater 2009;41:599–621. https://doi.org/10.1016/j.mechmat.2008.11.004.
[31] Johnson G.R. A constitutive model and data for materials subjected to large strains, high strain rates, and high temperatures. Proc 7th Inf Sympo Ballistics 1983:541–547.
[32] Khan AS, Huang S. Experimental and theoretical study of mechanical behavior of 1100 aluminum in the strain rate range 10−5−104s−1. Int J Plastic 1992;8:397–424. https://doi.org/10.1016/0749-6419(92)90057-J.
[33] Fields D, Backofen W. Determination of strain hardening characteristics by torsion testing. Proc ASTM 1957;57:1259–72.
[34] Molinari A, Ravichandran G. Constitutive modeling of high-strain-rate deformation in metals based on the evolution of an effective microstructural length. Mech Mater 2005;37:737–52. https://doi.org/10.1016/j.mechmat.2004.07.005.
[35] VOCE E. The relationship between stress and strain for homogeneous deformation. J Inst Metals 1948;74:537–62.
[36] Zener C, Hollomon JH. Effect of strain rate upon plastic flow of steel. J Appl Phys 1944;15:22–32. https://doi.org/10.1063/1.1707363.
[37] Khan AS, Zhang H, Takacs L. Mechanical response and modeling of fully compacted nanocrystalline iron and copper. Int J Plastic 2000;16:1459–76. https://doi.org/10.1016/S0749-6419(00)00023-1.
[38] Khan AS, Sung Suh Y, Kazmi R. Quasi-static and dynamic loading responses and constitutive modeling of titanium alloys. Int J Plastic 2004;20:2233–48. https://doi.org/10.1016/j.ijplas.2003.06.005.
[39] Khan AS, Suh YS, Chen X, Takacs L, Zhang H. Nanocrystalline aluminum and iron: mechanical behavior at quasi-static and high strain rates, and constitutive modeling. Int J Plastic 2006;22:195–209. https://doi.org/10.1016/j.ijplas.2004.07.008.
[40] Farrokh B, Khan AS. Grain size, strain rate, and temperature dependence of flow stress in ultra-fine grained and nanocrystalline Cu and Al: synthesis, experiment, and constitutive modeling. Int J Plastic 2009;25:715–32. https://doi.org/10.1016/j.ijplas.2008.08.001.
[41] Zerilli FJ, Armstrong RW. Dislocation-mechanics-based constitutive relations for material dynamics calculations. J Appl Phys 1987;61:1816–25.
[42] Voyiadjis GZ, Almasri AH. A physically based constitutive model for fcc metals with applications to dynamic hardness. Mech Mater 2008;40:549–63. https://doi.org/10.1016/j.mechmat.2007.11.008.
[43] Bodner SR, Partom Y. Constitutive equations for elastic-viscoplastic strain-hardening materials. J Appl Mech 1975;42:385–9. https://doi.org/10.1115/1.3423586.
[44] Lin YC, Zhang J, Zhong J. Application of neural networks to predict the elevated temperature flow behavior of a low alloy steel. Comp Mater Sci 2008;43:752–8. https://doi.org/10.1016/j.commatsci.2008.01.039.
[45] Lin YC, Chen X-M. A critical review of experimental results and constitutive descriptions for metals and alloys in hot working. Mater Des 2011;32:1733–59. https://doi.org/10.1016/j.matdes.2010.11.048.
[46] Rodríguez-Martínez JA, Pesci R, Rusinek A. Experimental study on the martensitic transformation in AISI 304 steel sheets subjected to tension under wide ranges of strain rate at room temperature. Mater Sci Eng A 2011;528:5974–82. https://doi.org/10.1016/j.msea.2011.04.030.
[47] Olson GB, Cohen M. Kinetics of strain-induced martensitic nucleation. MTA 1975;6:791. https://doi.org/10.1007/BF02672301.
[48] Stringfellow RG, Parks DM, Olson GB. A constitutive model for transformation plasticity accompanying strain-induced martensitic transformations in metastable austenitic steels. Acta Metallurgica et Materialia 1992;40:1703–16. https://doi.org/10.1016/0956-7151(92)90114-T.
[49] Iwamoto T, Tsuta T, Tomita Y. Investigation on deformation mode dependence of strain-induced martensitic transformation in trip steels and modelling of transformation kinetics. Int J Mech Sci 1998;40:173–82. https://doi.org/10.1016/S0020-7403(97)00047-7.
[50] Rodríguez-Martínez JA, Rusinek A, Pesci R, Zaera R. Experimental and numerical analysis of the martensitic transformation in AISI 304 steel sheets subjected to perforation by conical and hemispherical projectiles. Int J Solids Struct 2013;50:339–51. https://doi.org/10.1016/j.ijsolstr.2012.09.019.
[51] Kpenyigba KM, Jankowiak T, Rusinek A, Pesci R. Influence of projectile shape on dynamic behavior of steel sheet subjected to impact and perforation. Thin-Wall Struct 2013;65:93–104. https://doi.org/10.1016/j.tws.2013.01.003.
[52] Recht RF, Ipson TW. Ballistic perforation dynamics. J Appl Mech 1963;30:384–90. https://doi.org/10.1115/1.3636566.